JGR Oceans

RESEARCH ARTICLE
10.1029/2025JC022524

# Basal Melt Rate Variability and Tidal Current Vertical Structure From Observations Beneath Ronne Ice Shelf, Antarctica

**J. Anselin[1,2], K. W. Nicholls[1], P. R. Holland[1], J. R. Taylor[2], S. Østerhus[3], and K. Makinson[1]**

[1]British Antarctic Survey, Cambridge, UK, [2]Department of Applied Mathematics and Theoretical Physics, University of Cambridge, Cambridge, UK, [3]NORCE Norwegian Research Centre and Bjerknes Centre for Climate Research, Bergen, Norway

**Key Points:**

- Melt rate variability on spring-neap timescales is driven by fortnightly variations in both current speed and thermal driving
- Enhanced influence of ice base friction on the semidiurnal tidal ellipses due to proximity to their critical latitudes is observed directly
- Ice base friction-induced attenuation of both the tidal fluctuations and the mean tidal current magnitude increases during spring tides

**Supporting Information:**

Supporting Information may be found in the online version of this article.

**Correspondence to:**

J. Anselin,
joslin53@bas.ac.uk

**Citation:**

Anselin, J., Nicholls, K. W., Holland, P. R., Taylor, J. R., Østerhus, S., & Makinson, K. (2025). Basal melt rate variability and tidal current vertical structure from observations beneath Ronne Ice Shelf, Antarctica. *Journal of Geophysical Research: Oceans*, *130*, e2025JC022524. https://doi.org/10.1029/2025JC022524

Received 19 FEB 2025
Accepted 19 JUL 2025

**Author Contributions:**

**Conceptualization:** J. Anselin
**Data curation:** J. Anselin, K. W. Nicholls
**Formal analysis:** J. Anselin
**Funding acquisition:** K. W. Nicholls, S. Østerhus
**Methodology:** J. Anselin, J. R. Taylor
**Supervision:** K. W. Nicholls, P. R. Holland, J. R. Taylor
**Visualization:** J. Anselin
**Writing – original draft:** J. Anselin
**Writing – review & editing:** J. Anselin, K. W. Nicholls, P. R. Holland, J. R. Taylor, S. Østerhus, K. Makinson



**Abstract** This study examines the interplay between water column structure, tidal currents, and basal melting at a site beneath Ronne Ice Shelf, using a 3-year data set of oceanographic measurements, and a collocated year-long time series of radar-derived melt rate estimates. Currents at the site are characterized by mixed semidiurnal tides with strong spring-neap variability, superimposed on a nontidal flow. The product of current speed and thermal driving, both measured approximately 19 m from the ice base, explains 88% of the melt rate variability. Although current speed is the dominant driver of this variability, thermal driving also contributes non-negligibly on spring-neap and longer timescales. The semidiurnal tidal ellipses feature marked vertical variations, transitioning from nearly rectilinear in the mid-water column to more circular and clockwise (CW)-rotating near the ice. This depth-dependence of the semidiurnal tide is attributed to the differential influence of boundary friction on the CW and anticlockwise (ACW) rotary components near the critical latitude (where the tidal frequency equals the Coriolis frequency). A theoretical model, which assumes depth-independent eddy viscosity, successfully reproduces the observed 3-year mean vertical structure of the tidal ellipses. Considering the total tidal current rather than individual constituents, ice base friction damps both the time-mean flow speed and the tidal fluctuations, with attenuation varying over the spring-neap cycle, peaking during spring tides. The observed latitude- and time-dependent effects of ice base friction on the barotropic tide are not captured in parameterizations that estimate tide-induced friction velocity by scaling the time-averaged barotropic tidal speed with a constant drag coefficient.

**Plain Language Summary** Ice shelves are floating extensions of the Antarctic Ice Sheet that help slow the flow of grounded ice into the ocean. When these ice shelves thin due to melting at their base, known as basal melting, they become less effective at holding back grounded ice. This can lead to faster flow of grounded ice into the ocean, contributing to sea level rise. Understanding the processes that control basal melting is therefore essential for improving sea level rise projections. In this study, we use measurements of ocean properties and basal melting collected beneath one of Antarctica's largest ice shelves, to examine how melting varies over time, and how tides influence this variability. We find that variations in melt rates due to tides are predominantly caused by fluctuations in the current speed near the ice. Our data set also shows that tidal currents change with depth due to friction at the ice base and the effect of Earth's rotation, and that the extent of this frictional effect varies over time. Our study challenges assumptions underlying a formula that is applied in ocean models to represent the effect of tides on basal melt rates.

## 1. Introduction

Enhanced basal melting of Antarctic ice shelves reduces their buttressing ability, leading to an accelerated flux of upstream grounded ice into the ocean (Reese et al., 2018). This is considered the primary mechanism by which the Antarctic Ice Sheet is currently losing mass and contributing to sea level rise (Depoorter et al., 2013; Pritchard et al., 2012). To reduce uncertainty in projections of Antarctica's contribution to sea level rise, it is therefore critical to improve further our understanding of the complex interplay between ocean conditions and basal melting. A major challenge in studying ice shelf-ocean interactions is the broad range of timescale over which ocean conditions and basal melt rates vary, with the dominant drivers of temporal variability differing across timescales and between ice shelves (e.g., Davis et al., 2018; Hattermann et al., 2021; Vaňková & Nicholls, 2022).

As highlighted in a recent review by Rosevear, Gayen, and Galton-Fenzi (2022), the melt response to flow variability on short timescales, driven by processes such as tides, eddies, and internal waves, remains poorly understood. Here, we focus on the role of tides as a key driver of this variability. The strength of tidal currents varies around Antarctica, with some of the strongest tides present in the Weddell Sea, as shown by both modeling studies (e.g., Makinson & Nicholls, 1999; Richter et al., 2022) and in situ observations (e.g., Jenkins et al., 2010; Nicholls et al., 1997). In this region, tidal forcing comes predominantly from the semidiurnal tidal band, resulting in a fortnightly spring-neap cycle in the tidal currents at many locations beneath Ronne Ice Shelf (Vaňková & Nicholls, 2022).

Tidal currents are known to impact basal melting through numerous mechanisms, which may be broadly categorized into far-field and local processes (Padman et al., 2018). The far-field processes take place offshore and on the continental shelf (e.g., tide-induced sea ice motion, tidal rectification, and tidal contribution to ocean mixing) and they impact basal melt rates indirectly by modifying the thermohaline properties of the water masses entering the cavity. The local processes occur within the ice shelf cavity and they influence melt rates more directly by modulating the supply of heat to the ice base through tide-driven turbulent mixing within and below the ice shelf-ocean boundary layer.

Several numerical modeling studies have investigated the combined effect of far-field and local tidal processes on basal melt rates using idealized cavity geometries (Gwyther et al., 2016), single ice shelf simulations (Huot et al., 2021; Kim et al., 2023; Mueller et al., 2012), regional models (Arzeno et al., 2014; Hausmann et al., 2020; Jourdain et al., 2019; Makinson et al., 2011; Mueller et al., 2018; Robertson, 2013), and circum-Antarctic models (Richter et al., 2022). Most of these studies focused on quantifying the net effect of tides by comparing melt rates from simulations with and without tidal forcing. Jourdain et al. (2019) and Richter et al. (2022) went a step further by applying a dynamical-thermodynamical decomposition technique to distinguish between tide-induced basal melting due to tidal processes within and outside the ice shelf-ocean boundary layer. Both of these studies found that tides primarily impact basal melt rates by increasing current shear at the ice base, thus enhancing turbulent mixing within the ice shelf-ocean boundary layer. Although the above modeling studies have helped build a detailed picture of the spatial variability of tide-induced basal melting around Antarctica, their analyses were based on monthly to multi-year averaged simulation outputs, meaning that melt rate variability on shorter timescales was not resolved. As a result, the melt response to temporal variations in ocean conditions over the tidal and spring-neap cycle, as seen in large-eddy simulations of a tidally forced ice shelf-ocean boundary layer beneath Larsen C Ice Shelf (Vreugdenhil et al., 2022), were not captured in these studies.

Although high-temporal-resolution simulations, such as those presented by Vreugdenhil et al. (2022), provide valuable insights into the influence of high-frequency flow variability on ice shelf-ocean interactions, their idealized set up may neglect certain processes that could be important, and the results may be sensitive to the melt rate parameterization. An alternative and complementary approach is to combine in situ oceanographic observations with collocated basal melt rate measurements at sufficiently high temporal resolution. High-resolution basal melt rate time series can be obtained from upward-looking sensors deployed through boreholes (Nixdorf et al., 1994) or via surface-based radar techniques (Corr et al., 2002; Nicholls et al., 2015). Although such local basal melt rate measurements remain scarce, they have been successfully combined with oceanographic observations at sites where tides are present, including beneath Amery Ice Shelf (Rosevear, Galton-Fenzi, & Stevens, 2022), west of Korff Ice Rise beneath Ronne Ice Shelf (Jenkins et al., 2010), and multiple locations beneath Filchner-Ronne Ice Shelf (Vaňková & Nicholls, 2022). However, these studies primarily examined the time-averaged effects of tides, typically based on monthly or yearly means. As a result, the melt response to ocean variability on timescales shorter than one month remains poorly constrained by observations.

Robertson (2013) proposed that the spatial variations in tide-induced basal melting observed in their regional model simulations may be linked to enhanced tidal vertical mixing near the critical latitude (the latitude at which the tidal frequency equals the Coriolis frequency). This hypothesis aligns with results from Makinson (2002), who used a one-dimensional turbulence closure model thermodynamically coupled to an ice shelf to simulate tidal currents and mixing beneath Ronne Ice Shelf, demonstrating that boundary friction has a stronger influence near the critical latitude, leading to thicker bottom and under-ice boundary layers. Consistent with this, observations by Foldvik et al. (2001) and Makinson et al. (2006) seaward of Ronne Ice Front (see Figure 1) revealed tidal currents exhibiting marked variation with depth near the seabed. There is also a large body of literature reporting on observations of strongly depth-dependent tidal currents in mid-latitude shelf seas (e.g., Kopte et al., 2022; Maas &

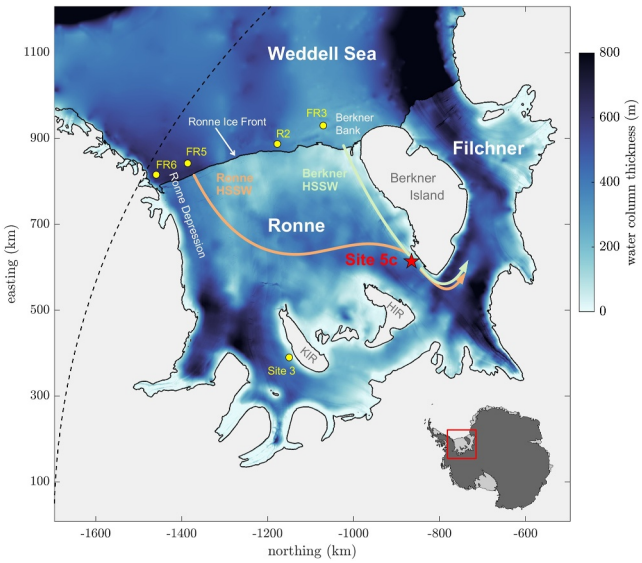


**Figure 1.** Map of the southern Weddell Sea including Filchner Ice Shelf and Ronne Ice Shelf. The color shading shows water column thickness, with the colormap saturated at 800 m (data from BedMachine, Morlighem et al., 2017). Site 5c borehole location is indicated by the red star marker. The yellow circle markers indicate Site 3 borehole location (Jenkins et al., 2010), and FR6, FR5, R2, and FR3 ocean mooring locations (Foldvik et al., 2001; Makinson et al., 2006). The geographic labels KIR and HIR indicate Korff Ice Rise and Henry Ice Rise, respectively. The orange and green arrows show schematic representation of the flow of Ronne and Berkner High-Salinity Shelf Water toward Site 5c. The $M_2$ critical latitude is marked by the black dashed line.

van Haren, 1987; Simpson & Tinker, 2007; Souza & Simpson, 1995; Verspecht et al., 2010; Visser et al., 1994). However, the influence of friction along the ice base on tidal current profiles beneath Antarctic ice shelves has not yet been described using observational data.

To complement existing studies of tidal effects and address the observational gaps described above, the present study examines basal melt rate variability and tidal currents using in situ oceanographic and melt rate measurements beneath Ronne Ice Shelf. Specifically, we aim to (a) assess variability in water column properties and basal melt rate across multiple timescales, with a focus on tidal to spring-neap variations, and (b) investigate the influence of ice base friction on the vertical structure of tidal currents. The analyses are based on a unique 3-year long observational record of ocean properties from Site 5c (see red marker in Figure 1), obtained from instruments deployed through a hot-water drilled borehole. We combine these data with an overlapping and collocated, previously published year-long basal melt rate time series derived from surface-based radar measurements (Vaňková & Nicholls, 2022). Previous surveys at Site 5c have identified a tidal signal dominated by the semidiurnal constituents $M_2$ and $S_2$ (Nicholls et al., 2001), and the site is located near their respective critical latitudes. Combined with the availability of in situ melt rate and oceanographic measurements, this makes Site 5c particularly well suited for examining tidal processes, and their impact on melt rates, in the vicinity of a critical latitude.

The remainder of this paper is structured as follows. Section 2 describes the study site, the sub-ice shelf mooring configuration, and the methods used to obtain the basal melt rate time series. In Section 3, we provide an overview of the hydrographic and melt rate observations, including an assessment of the dominant timescales of variability. Section 4 examines the local drivers of basal melting variability, followed by an investigation of the tidal current vertical structure in Section 5. Finally, Section 6 summarizes the key findings and discusses their implications.

## 2. Data and Methods

### 2.1. Study Site

This study makes use of long-term oceanographic and glaciological observations made at Ronne Ice Shelf Site 5c (S 80°15.53, W 54°38.73). The cavity circulation beneath Ronne Ice Shelf is predominantly driven by High-Salinity Shelf Water (HSSW), a cold and dense water mass generated from brine rejection during sea ice formation seaward of the ice front (Nicholls et al., 2001). The study site is located 18 km west of the southwest coast of Berkner Island and approximately 300 km from the nearest ice front (see map in Figure 1). It is positioned ~6° south of the critical latitude of the $M_2$ tidal constituent (S 74°28.31) and ~6°north of the $S_2$ critical latitude (S 85° 45.91), with critical latitude defined as the latitude at which the tidal frequency equals the Coriolis frequency. The oceanographic data set was obtained from instruments deployed through a hot-water drilled access hole. At the time of drilling (January 2015), the ice thickness at the location was 740 m, the snow surface elevation was 80 m above sea level, and the sea floor depth was 1,038 m below sea level, implying a 370 m water column thickness.

### 2.2. Field Observations

#### 2.2.1. Oceanographic Observations via a Hot-Water Drilled Borehole

To deploy oceanographic instruments beneath the ice shelf, an access hole was drilled with hot water. Within 24 hr of drilling the access hole, a set of ten conductivity-temperature (CT)-depth (CTD) profiles were collected through the sub-ice shelf water column using an SBE 49 FastCAT CTD profiler. After post-calibration of the instrument, the raw data were quality controlled to remove obviously erroneous spikes, corrected for thermal inertia of the conductivity cell, and averaged into 1 m vertical bins using the Seabird processing software.

**Table 1**
*Overview of the Sub-Ice Shelf Mooring Measurements and ApRES-Derived Basal Melt Rate Measurements Used for This Study*

| | Instrument | Depth (m) | Dist. from ice (m) | Duration (days) |
|---|---|---|---|---|
| | ApRES | ~ | ~ | 375 |
| CT1 | SBE 37 MicroCAT | 679 | 19 | 1,096 |
| CM1 | Nortek Aquadopp 3,000 m | 679 | 19 | 1,096 |
| CT2 | RBR duo CT | 698 | 38 | 1,096 |
| CT3 | RBR duo CT | 745 | 85 | 1,096 |
| CT4 | RBR duo CT | 815 | 155 | 1,096 |
| CM4 | Nortek Aquadopp 3,000 m | 815 | 155 | 1,096 |
| CT5 | RBR duo CT | 916 | 256 | 1,096 |
| CT6 | SBE 37 MicroCAT | 1,029 | 369 | 1,096 |

*Note.* The depths values (column 3) correspond to the depth below sea level; the distance from the ice base (column 4) is given with respect to the ice base depth at the time of deployment (January 2015).

Following the CTD casts, a mooring was permanently deployed through the access hole. A ballast weight was attached to the bottom of the mooring line to minimize swinging due to ocean currents. The results presented in this paper are based on data collected by six CT sensors (CT1−CT6) and two current meters (CM1 and CM4), including two CT/CM instrument clusters positioned at approximately 19 and 155 m from the ice base (CT1/CM1 and CT4/CM4, respectively). The instrument model types and deployment depths are listed in Table 1. The instruments sampled at 2-hourly intervals. The data were communicated via the mooring cable to a solar-powered data logger located at the surface of the ice shelf, and transferred in near real-time using an Iridium satellite data link. The mooring data presented in this paper are based on measurements taken over the 3-year period spanning from the 15$^{th}$ January 2015 to the 15$^{th}$ January 2018.

The temperature and conductivity sensors were manufacturer-calibrated before deployment and the stated accuracy of the sensors is ±0.002°C and ±0.003 mS/m, respectively. To align with modern practice and facilitate comparison with recent observational studies (e.g., Hattermann et al., 2021), temperature and salinity data presented in figures are shown in terms of conservative temperature (unit: °C, notation: $\Theta$) and absolute salinity (unit: g kg$^{-1}$, notation: $S_A$). To convert in situ temperature, $T$, and practical salinity, $S$, to $\Theta$ and $S_A$, respectively, we use the TEOS-10 Gibbs Seawater MATLAB package (McDougall & Barker, 2011). The velocity components measured by CM1 and CM4 have been transformed into a geographically aligned horizontal reference frame with $u$ defined positive east and $v$ positive north. Note that the coast of Berkner Island is oriented approximately 10° east of true North. All the time series have been interpolated onto common hourly sample times to match the sampling frequency of the basal melt rate observations (see next section). Filtered data presented in this paper are obtained by applying a 4th-order low-pass digital Chebyshev Type I filter.

### 2.2.2. Basal Melt Observations From an ApRES

In addition to the oceanographic mooring data, we make use of a year-long time series of basal melt rates inferred from autonomous phase-sensitive radio echosounder (ApRES) measurements (Brennan et al., 2014). The ApRES instrument used to derive this time series was deployed at Site 5c in January 2015. The unit was placed on the ice shelf surface approximately 15 m from the access hole through which the mooring had been deployed. The ApRES captured a full year of data at an hourly sampling rate before being recovered in January 2016.

A detailed description of the approach used to infer the melt rate time series from the Site 5c 2015 ApRES measurements can be found in Vaňková et al. (2020), with key steps outlined here. Following the methodology developed by Nicholls et al. (2015), a time series of total ice shelf thinning rate was derived by taking the time-derivative of the distance between the radar antennas and the ice shelf base detected by the radar. The nonmelt-related effects (ice column vertical strain and firn compaction), determined by tracking vertical motion of internal reflection horizons, were subtracted from the total thinning rates to give the ApRES-derived basal melt rate time series. At diurnal and higher frequencies, the amplitude of the tidal signal in the total thinning rate is very well

determined because of the high signal to noise ratio of that reflection. However, the uncertainty in the vertical strain rate signal at tidal frequencies is relatively large (Vaňková et al., 2020), making it difficult to extract nonmelt-induced thickness variations caused by the ice shelf compressing and extending at tidal frequencies. To overcome this difficulty, the total thinning rate signal was low-pass filtered using a 36-hr cutoff and the vertical strain rate was averaged over the year under the assumption that there is insignificant variability in the strain rate contribution at timescales longer than tidal, which would otherwise contaminate the inferred melt rate time series (in particular, it was confirmed that the strain rates contained no measurable fortnightly signal). Note that this processing removes diurnal and semidiurnal variability in the inferred basal melt rates. The estimated uncertainty in the mean inferred melt rate is $\pm 0.1$ m yr$^{-1}$, with most of the uncertainty resulting from uncertainty in the derived strain rate (Vaňková et al., 2020).

### 2.3. Basal Melt Rate Parameterization

In order to obtain a record of concurrent ocean properties and melt rate over the 3-year mooring record, we extend the basal melt rate time series derived from 2015 ApRES measurements using a basal melt rate parameterization. We achieve this by first tuning the parameterization to replicate the observed ApRES-derived melt rates over the year 2015. We then apply the calibrated parameterization to the ocean measurements from the uppermost mooring sensors to estimate melt rates beyond 2015. The remainder of this section describes the basal melt rate parameterization calibration steps in more detail.

The melt rate at the base of an ice shelf, $m$, can be diagnosed by solving a system of three equations that describe the conservation of heat, the conservation of salt, and the freezing point of seawater at the ice-ocean interface (McPhee et al., 1987). Various forms of this three-equation model, which mostly differ in their approaches to parameterizing the turbulent heat and salt fluxes through the ice shelf-ocean boundary layer, have been proposed (Rosevear et al., 2024). Here we employ the shear-dependent formulation recommended by Jenkins et al. (2010), in which the oceanic heat and salt fluxes are calculated as a function of the friction velocity, the bulk temperature and salinity changes across the boundary layer, and constant, observationally derived transfer coefficients for heat and salt ($\Gamma_T$ and $\Gamma_S$). Assuming that a relatively homogeneous mixed layer develops below the millimeter-scale viscous sublayer, and that the friction velocity is related to the free-stream current speed outside of the logarithmic layer, $U_M$, through the quadratic drag expression as follows:

$$u_* = \sqrt{C_d}\, U_M \,, \tag{1}$$

with $C_d$ a constant drag coefficient, then the three-equation formulation takes the following form:

$$\rho_i\, m\, L_i = \rho_i\, c_i\, m\, (T_i - T_b) - \rho_w\, c_w \sqrt{C_d}\, \Gamma_T\, U_M\, (T_b - T_M) \,, \tag{2}$$

$$\rho_i\, m\, (S_b - S_i) = -\rho_w \sqrt{C_d}\, \Gamma_S\, U_M\, (S_b - S_M) \,, \tag{3}$$

$$T_b = \lambda_1\, S_b + \lambda_2 + \lambda_3\, p_b \,, \tag{4}$$

where $\rho$ is density, $L$ is latent heat of fusion, $c$ is specific heat capacity, $T$ is in situ temperature, $S$ is practical salinity, and $p$ is pressure; with the subscripts $i$, $b$, and $M$ referring to ice, ice shelf base, and mixed layer, respectively. $\lambda_1$, $\lambda_2$, $\lambda_3$ are empirical constants chosen to optimize the assumed linear fit between the seawater freezing point and both salinity and pressure. The values of the constants are listed in Table 2. The conductive heat flux through the ice shelf (first term on the right-hand side of Equation 2) is parameterized here following Nøst and Foldvik (1994). Assuming constant thermal and haline Stanton numbers ($\sqrt{C_d}\Gamma_T$ and $\sqrt{C_d}\Gamma_S$, respectively) and a heat to salt transfer coefficient ratio of $\Gamma_T/\Gamma_S = 35$ (Jenkins et al., 2010), Equations 2–4 can be solved for either $\sqrt{C_d}\Gamma_T$ or $m$ (assuming the other is known), without prior knowledge of $T_b$ and $S_b$, quantities that are very difficult to observe. Note that Equations 2–4 are applied using $T$ and $S$ (as opposed to $\Theta$ and $S_A$) as the empirical coefficients embedded in the formulation were originally derived with those variables. Although converting the formulation to TEOS-10 would have negligible impact on the estimated melt rates, it would alter the inferred Stanton numbers, complicating comparison with previous studies that almost exclusively use $T$ and $S$ in the three-equation formulation (e.g., Davis & Nicholls, 2019; Jenkins et al., 2010; Malyarenko et al., 2020).

**Table 2**
*Constant Parameter Values Applied in the Three-Equation Formulation (Equations 2–4)*

| Parameter | Symbol | Value |
|---|---|---|
| Freezing point salinity coefficient | $\lambda_1$ | $-5.73 \times 10^{-2}$ °C |
| Freezing point offset | $\lambda_2$ | $8.32 \times 10^{-2}$ °C |
| Freezing point depth coefficient | $\lambda_3$ | $-7.53 \times 10^{-8}$ °C Pa$^{-1}$ |
| Specific heat capacity of seawater | $c_w$ | 3,974 J kg$^{-1}$ °C $^{-1}$ |
| Reference seawater density | $\rho_w$ | 1,030 kg m$^{-3}$ |
| Specific heat capacity of ice | $c_i$ | 2,009 J kg$^{-1}$ °C $^{-1}$ |
| Latent heat of fusion of ice | $L_i$ | $3.34 \times 10^5$ J kg$^{-1}$ |
| Temperature of ice | $T_i$ | −25 °C |
| Salinity of ice | $S_i$ | 0 psu |

We first solve for $\sqrt{C_d}\Gamma_T$ to calibrate the parameterization to Site 5c conditions observed in 2015. Applying the ApRES melt rate record from 2015 and the concurrent 36-hr low-pass filtered temperature, salinity and current speed time series measured by CT1 and CM1 over the same period, yields a median thermal Stanton number of 0.0006. This value corresponds to approximately half the value derived by Jenkins et al. (2010) based on data collected at a different site under Ronne Ice Shelf (Site 3, see Figure 1). Similarly to the Site 5c mooring design, the uppermost CM at Site 3 was located approximately 20 m from the ice base. However, the uppermost CT sensor at Site 3 was located much closer to the ice base than CT1 in the Site 5c mooring design (~2 m vs. ~19 m from the ice base). Based on the mean temperature profile from the pre-deployment CTD casts, which reveals a thermal mixed layer that is not fully homogenized (Figure 2a), evaluating $T_M$ at ~2 m from the ice base versus ~19 m from the ice base, with all other parameters remaining unchanged, would approximately double the derived thermal Stanton number. This suggests that the difference in derived thermal Stanton number between the two Ronne sites largely reflect the differences in placement of the uppermost temperature sensor relative to the ice base, rather than differences in boundary layer properties. Nonetheless, we note that the upper water column structure at Site 5c is atypical (as will be described in Section 3.1), which complicates the comparison.

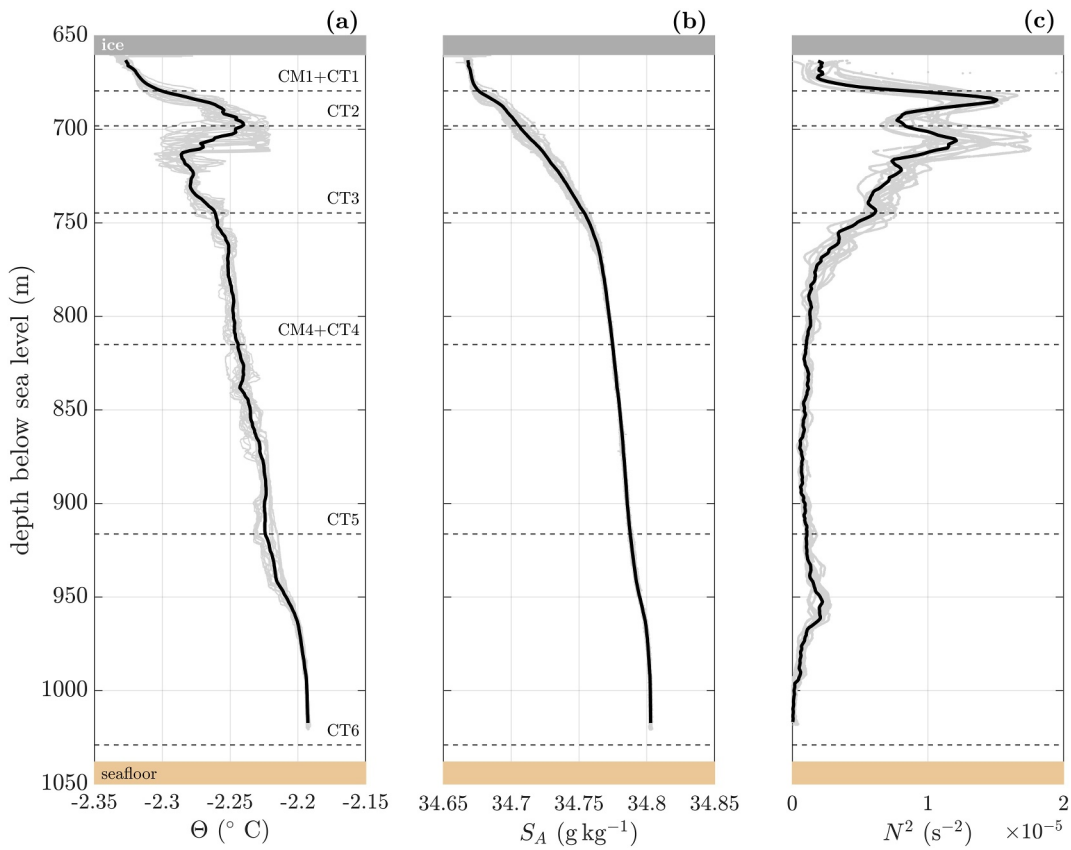


**Figure 2.** (a) Vertical profiles of conservative temperature (Θ), (b) absolute salinity ($S_A$), and (c) buoyancy frequency squared ($N^2$) from data collected during the CTD casts taken just before the January 2015 mooring deployment at Site 5c (red star marker in Figure 1). Thin gray lines indicate depth-binned profiles from the individual casts and thick black lines correspond to the ten-profile mean. The dashed horizontal lines show the position of the moored current meters and conductivity-temperature sensors. The ice shelf base is indicated by the shaded gray box with the depth of the ice base corresponding to the January 2015 depth and the seabed is indicated by the shaded brown box.

After obtaining the median $\sqrt{C_d}\Gamma_T$ for the year 2015, we use this value to compute a time series of $m$ for the 3-year record by applying the calibrated parameterization to the 36-hr low-pass filtered hydrographic measurements from CT1 and CM1. Note that this implicitly assumes that the mean scalar and velocity boundary layer structure between the uppermost instrument cluster and the ice base is representative of the time-varying boundary layer structure throughout the 3-year period. Figure A1 shows the distribution of the resulting melt rate estimate as a function of the ApRES-derived melt rates for the year 2015. The correlation coefficient squared is equal to 0.88 indicating an acceptable reproduction of the measured variability by the tuned parameterization. Considering monthly timescales further improves the match, with an $r^2$ of 0.98 between the 30-day low-pass filtered parameterized and ApRES-derived melt rate time series.

## 3. Observed Hydrography and Melting

Building on previous investigations of the hydrography and basal melt rates beneath Ronne Ice Shelf (e.g., Hattermann et al., 2021; Nicholls et al., 2001; Vaňková et al., 2020; Vaňková & Nicholls, 2022), we present a detailed characterization of Site 5c based on the 3-year ocean properties and basal melt rate time series introduced in the previous section. This includes a description of the water column structure, a characterization of the current forcing, an overview of the basal melt rate record, and an assessment of the variability of the measured properties on timescales shorter than one month, all aimed at providing important context for interpreting the results presented in Sections 4 and 5.

### 3.1. Water Column Structure

We start by describing the water column structure based on the sequence of CTD casts performed prior to the mooring deployment, before examining how some of the characteristics identified from the CTD profiles may vary over the 3-year long mooring record.

Figure 2 shows the mean 1 dbar-binned vertical profiles (thick black lines) from the pre-mooring deployment CTD casts. The profiles from the individual CTD casts are also shown (thin gray lines) to give an indication of the water column structure variability over the 5.5 hr-long sampling period. Salinity being the dominant determinant of density in polar oceans, the mean $S_A$ profile reveals a ∼20-m-thick layer of relatively uniform density beneath the ice base, which we henceforth refer to as mixed layer. The top mooring sensor was positioned just inside the mixed layer at the time of deployment. Within the mixed layer, the mean temperature is ∼−2.32°C. This corresponds to ∼0.08°C thermal driving, with thermal driving defined here as the temperature above the local freezing point calculated using pressure at the ice base.

The mean temperature profile indicates a warm feature just beneath the ice base, extending to approximately 725 m below sea level (∼65 m from the ice base). This warm feature was identified in CTD profiles collected at the same site in January 1999 (Nicholls et al., 2001), and it was interpreted as a warm water mass intruding at the top of the water column by Ekman transport along the ice shelf base, with the near-ice layer cooled by basal melting. This warm feature appears to be site-specific, having not been observed at other locations beneath Ronne Ice Shelf (Jenkins et al., 2010; Nicholls et al., 2001). Aside from the depth interval featuring the warm feature, there is an overall increase in temperature with depth with a maximum $\Theta$ of ∼−2.19°C near the seafloor. Salinity increases with depth over the entire vertical profile indicating stable stratification. As expected based on the relatively uniform water column density (total range in $S_A$ not exceeding 0.14 g kg$^{-1}$), the stratification at Site 5c is relatively weak with depth-mean stratification $N^2 \sim 5.8 \times 10^{-6}$ s$^{-2}$ between CT1 and CT4, where $N = \left[(-g/\rho_w)(\partial\rho/\partial z)\right]^{1/2}$ is the buoyancy frequency. The two pronounced peaks in $N^2$ visible in the upper water column (at around 683 and 705 m below sea level) reflect the increased salinity gradient at the base of the mixed layer and at the bottom of the warm feature, respectively. The individual profiles highlight a greater level of variability in the upper water column compared with deeper in the water column, with the base of the warm feature moving up and down by ∼20 m during the CTD profiling session.

The water masses present in the water column can be inferred by plotting the mean CTD data in $\Theta - S_A$ space (dark red markers in Figure 3). In line with the description of the water column presented by Nicholls et al. (2001), all the measurements are below the surface freezing temperature $\Theta_f(p = 0)$, indicating that the entire water column is Ice Shelf Water (ISW), that is, HSSW that has been modified either through direct interaction with the ice shelf base or through mixing with water masses that have had such interaction (Foldvik et al., 1985).

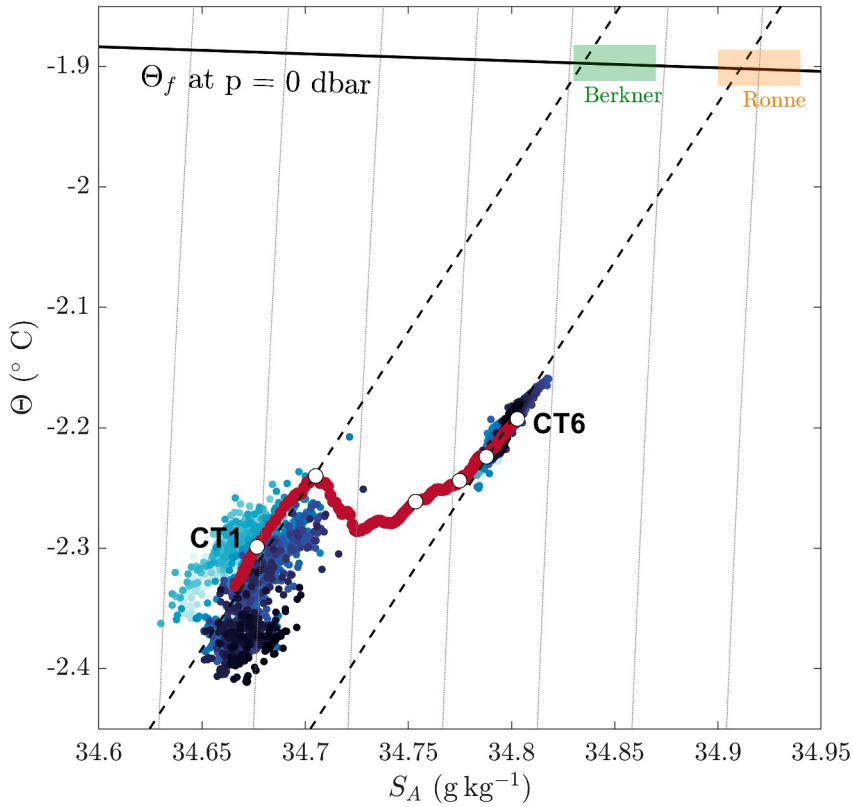


**Figure 3.** Oceanographic data from the mean CTD profiles plotted in $\Theta - S_A$ space (dark red markers). The white markers indicate the depths of the conductivity-temperature (CT) sensors on the CTD profile trace. Also shown are the first year of measurements collected by the mooring CT sensors at 679 and 1,029 m depth below sea level (CT1 and CT6, respectively) colored by time (light blue to dark blue as time progresses). The gray dashed contours show potential density. The black solid line indicates the freezing temperature of seawater at surface ($p = 0$ dbar). The black dashed lines indicate the meltwater mixing lines with gradient $d\Theta/dS_A = 2.63\ ^\circ C/g kg^{-1}$ calculated following McDougall et al. (2014). The green and orange patches indicate the high-salinity shelf water source salinity ranges as per Hattermann et al. (2021).

When freshwater ice melts and mixes into seawater, the properties of the resulting meltwater fall on a straight line in temperature-salinity space (Gade, 1979). Furthermore, HSSW is formed from brine rejection during sea ice production and its temperature can therefore be assumed to be at the surface freezing point. The salinity of the parent HSSW of a parcel of ISW with given $\Theta - S_A$ properties can therefore be estimated by extrapolating the meltwater mixing line (dashed lines in Figure 3) to its intersection with the surface freezing line (solid line in Figure 3). Ship-based observations have shown that the salinity of HSSW varies along Ronne Ice Front (e.g., Akhoudas et al., 2020; Gammelsrød et al., 1994; Janout et al., 2021). The estimated salinity of the source HSSW can hence be used to identify its likely origin along the ice front. Using the same HSSW source salinity ranges as applied by Hattermann et al. (2021), this analysis suggests that the water mass associated with the warm feature identified in the upper water column in Figure 2a corresponds to ISW derived from HSSW formed at Berkner Bank (Berkner HSSW; Figure 1), and that the upper part of this feature (adjacent to the ice base) has been cooled and freshened by interaction with the ice. Below CT2, there is a sharp transition to the deeper part of the water column likely originated from denser HSSW formed further away from Site 5c in the Ronne Depression (Ronne HSSW; Figure 1). This is consistent with the parent water masses inferred by Nicholls et al. (2001) based on Site 5 observations from the year 1999. In the mid-water column, between CT2 and CT5, $\Theta - S_A$ properties do not follow a meltwater mixing line, suggesting mixing between the meltwater-modified Berkner HSSW and Ronne HSSW.

The seasonal variability of the water column structure is illustrated in Hovmöller plots generated from the 30-day low-pass filtered mooring measurements at the six CT sensors (Figure 4), where the red dashed contours correspond to the temperature and salinity at the base of the mixed layer at the time of the CTD survey in January 2015. Figure 4a shows that the mid-water column, between CT2 and CT5, alternates between periods of relatively weak

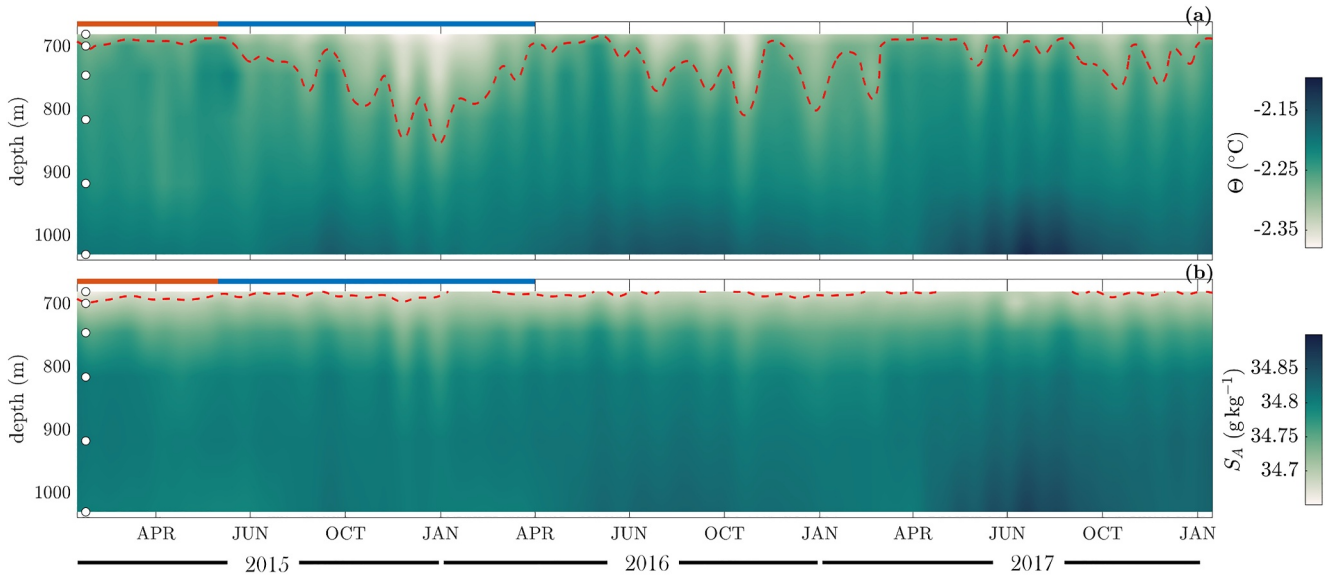


**Figure 4.** Evolution of the vertical profiles of (a) conservative temperature and (b) absolute salinity constructed from the moored conductivity-temperature sensor measurements over the 3-year observational period spanning January 2015–January 2018. The data were smoothed using a 30-day low-pass filter. The white markers indicate the mooring instrument depths. The red dashed contours indicate the (a) temperature and (b) salinity at the base of the mixed layer, as identified in the pre-mooring deployment mean CTD profiles (−2.27°C and 34.69 g kg$^{-1}$ respectively). The orange and blue horizontal lines indicate the periods January–May 2015 and May 2015–April 2016 mentioned in the text.

thermal gradient (e.g., January–May 2015, as indicated by the orange horizontal line) and periods of stronger thermal gradient (e.g., May 2015–April 2016, as indicated by the blue horizontal line). This low-frequency variability is further highlighted in the temperature profiles constructed from the mooring measurements (Figure 5a), where the orange and blue profiles have been constructed based on the mean temperature recorded by CT1-CT6 during the periods of weak and strong thermal gradient, respectively. In comparison with temperature, the salinity, and hence the density structure, exhibits very weak variations in the middle portion of the water column (Figures 4b and 5b). This suggests that the observed low-frequency variations of the mid-water column structure are linked with changes in water mass spiciness rather than being caused by heaving of the water column.

Although the mooring profiles might miss features occurring between sensors, comparing the mean mooring profiles January–May 2015 and May 2015–April 2016 with the mean CTD profile from January 2015 in Figure 5a reveals differences in the upper water column between the two periods. It is worth noting that the warm feature below the ice base, evident in the CTD profile, appears to be either absent, or at least too thin to be detected by CT1 when the thermal gradient is stronger in the mid-water column. Conversely, this warm feature appears to be more pronounced during periods of weaker mid-water column thermal gradient. Assuming that the ice shelf base remains at the freezing point, this suggests that the thermal gradient in the upper water column is increased during periods of weaker mid-water column thermal gradient.

To investigate the source of the upper water column variability visible in the Hovmöller diagram, we plot the temperature and salinity measurements from the first year of data collected by CT1 in $\Theta - S_A$ space (Figure 3), with the markers colored by time (light blue to dark blue as time progresses from January 2015 to January 2016). This suggests that the variations in the upper part of the water column may be due to changes in the salinity of the Berkner HSSW (the darker markers can be traced back to the upper end of the Berkner HSSW salinity range). An alternative interpretation for the source of the cold water that appears to replace the warm feature during certain periods of the time series, could be that when HSSW ceases to be produced over Berkner Bank around the end of October (Renfrew et al., 2002), recirculated ISW flows along the coast of Berkner Island and is transported to the mooring site in the upper portion of the water column, similarly to the ISW recirculation inferred by Nicholls et al. (2001). Although both mechanisms are plausible, the Hovmöller plot in Figure 4a appears to support the latter more strongly. However, further investigation into the exact mechanisms causing the observed seasonal variability of the upper water column would require additional data sets and is outside the scope of this paper.

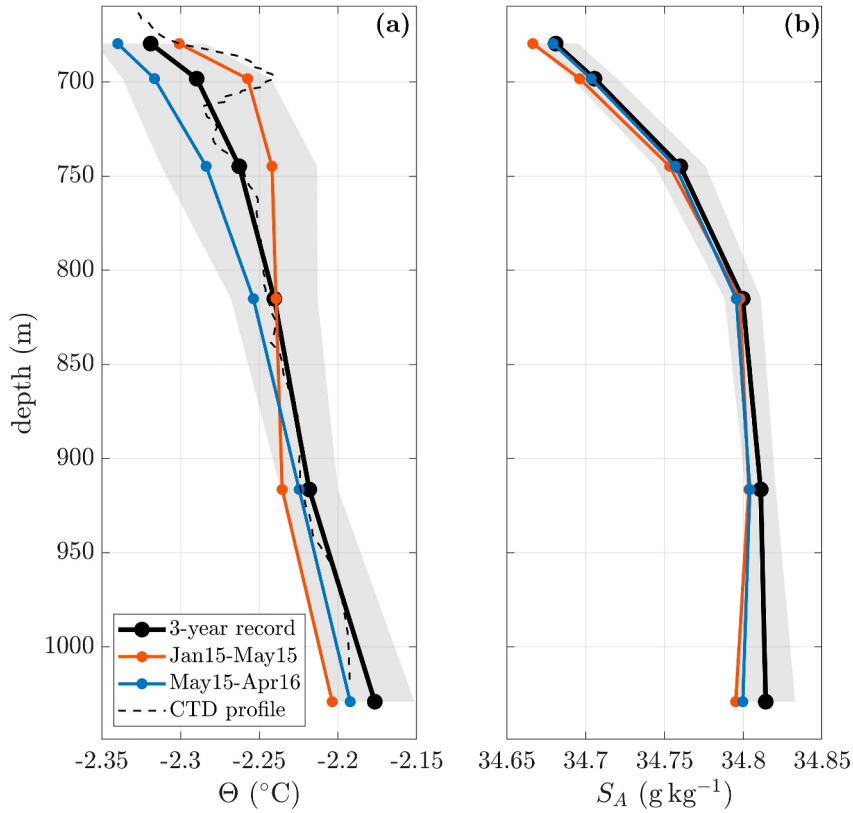


**Figure 5.** Average profiles of (a) conservative temperature and (b) absolute salinity, computed from the six conductivity-temperature mooring sensor records (position of sensors indicated by the markers). Black profiles indicate the mean over the 3-year record with gray shading showing one standard deviation either side of the mean. Orange and blue profiles correspond to the mean over the periods January 2015–May 2015, and May 2015–April 2016, respectively (as indicated by the same-colored horizontal lines in Figure 4). Also shown in (a) is the mean profile from the pre-deployment CTD casts performed in January 2015 (black dashed profile).

Figure 4a also shows that low-frequency temperature variability is more pronounced in the upper water column (at CT1 and CT2) compared with deeper down (at CT5 and CT6). This is further highlighted by comparing the mooring data from CT1 and CT6 plotted in $\Theta - S_A$ space (Figure 3). As suggested by Vaňková and Nicholls (2022), the upper intensification of the seasonal temperature signal at Site 5c may be traced back to the greater proximity of the upper HSSW to its source near Berkner Island (Figure 3). The small $\Theta - S_A$ variations in the deep water are likely to be a result of changes in Ronne HSSW production (given that the data points move up and down the same mixing line).

### 3.2. Currents

We now characterize the local dynamics based on data collected at the two CMs, CM1 and CM4, located at the same depth as the CT sensors CT1 (positioned near the outer edge of the mixed layer) and CT4 (positioned just above the Ronne-sourced portion of the water column). We also include here a description of the local tidal signal, with a more in-depth analysis of the tidal current vertical structure provided in Section 5.

As shown by the light gray curves in Figures 6a and 6b, the currents have absolute speeds $U = \sqrt{u^2 + v^2}$ ranging between $\sim$5 cm s$^{-1}$ and $\sim$30 cm s$^{-1}$. Similarly to the temperature variations noted in the previous section, the 30-day low-pass filtered velocity signals display a certain level of seasonal variability at both the upper and lower CMs (black curves in Figures 6a and 6b), with reduced current magnitude during the austral spring/summer months. Consistent with the low-frequency variability in mid-water column thermal structure described in Section 3.1, there is a strong correlation between the 30-day low-pass filtered current magnitude and temperature

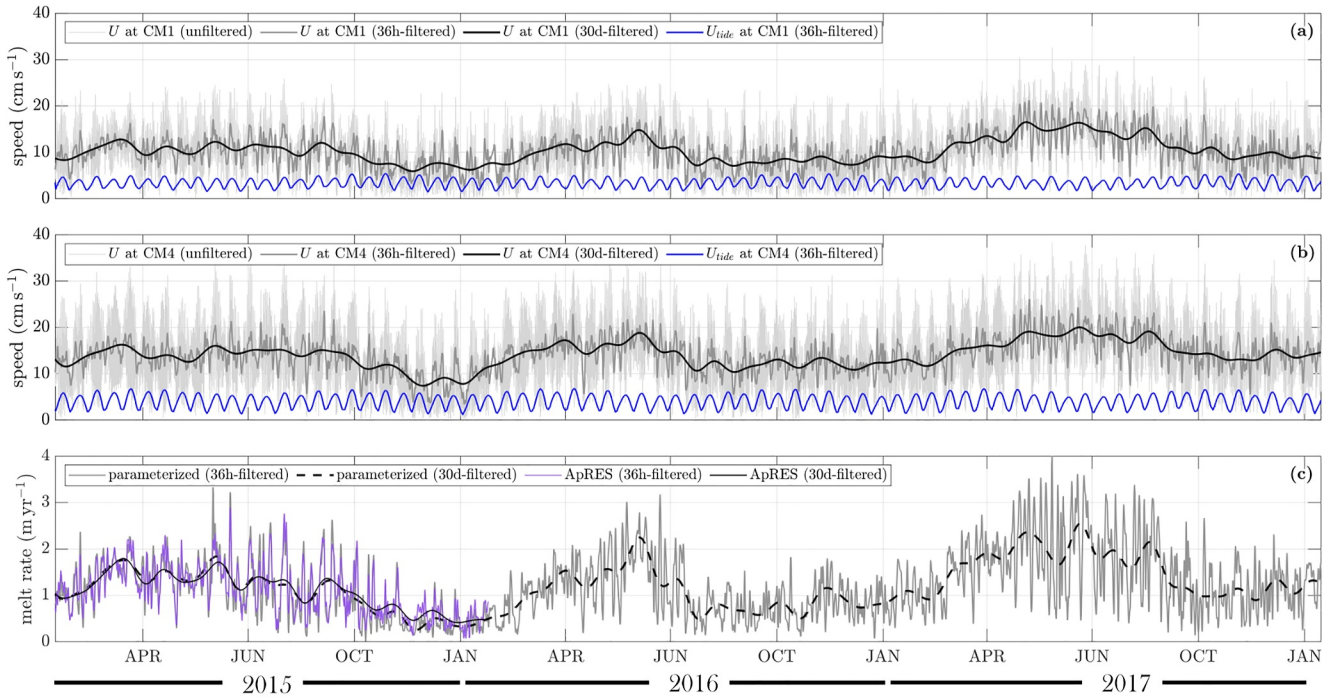


**Figure 6.** Overview of the records of current speeds and basal melt rates spanning the period January 2015–January 2018. (a, b) Total current speed $U$ and tidal current velocity $U_{tide}$ from CM1 (a) and CM4 (b), with low-pass filter cutoff values indicated in the legend labels. (c) ApRES-derived and parameterized basal melt rates, with low-pass filter cutoff values indicated in the legend labels.

at CM4/CT4 ($r = 0.79$), with periods of weak thermal gradient coinciding with stronger flow, and more strongly stratified periods coinciding with when the flow is weaker.

Figures 6a and 6b also shows that the current magnitudes at CM1 and CM4 exhibit similar variability, particularly at low frequencies, as seen when comparing the 30-day low-pass filtered time series. This qualitative observation is confirmed by the complex correlation between the complex velocity time series, which has a magnitude of 0.79 for the unfiltered data and 0.96 for the 30-day low-pass filtered time series. The phase of the complex correlation is equal to 3° for the unfiltered data, indicating that the flow variability is vertically coherent not only in magnitude but also in direction. Assuming that CM1 is positioned within the mixed layer, the strong vertical coherence in flow variability suggests that the near-ice current at this site is primarily driven by external forcing rather than by buoyant meltwater.

In order to identify the dominant tidal constituents, evaluate their mean tidal ellipse properties, and estimate the tidal current velocity, we perform a harmonic analysis of the currents measured by CM1 and CM4 over the 3-year observational period using the MATLAB package T_TIDE (Pawlowicz et al., 2002). We include all the tidal constituents accounted for in the package except for the solar semi-annual (*Ssa*) and solar annual (*Sa*) constituents, as these introduced a spurious seasonal signal into the derived tidal velocity time series. The harmonic analysis indicates that the tidal signal is dominated by the semidiurnal constituents $M_2$ and $S_2$ and by the diurnal constituents $K_1$ and $O_1$, as expected following previous tide related observational studies beneath and near Ronne Ice Shelf (Foldvik et al., 2001; Makinson et al., 2006; Vaňková et al., 2020). The rotary nature of each constituent's tidal ellipse is quantified in terms of its elliptic properties, namely the semi-major and semi-minor axes $a$ and $b$, inclination $\Psi$, and phase $\Phi$ (Foldvik et al., 2001; Makinson et al., 2006). The polarization, $P = b/a$, can be used to define the shape of the tidal ellipse, with the sense of rotation set by the sign of $b$ (given that $a$ is always positive). Definitions of each of these properties are given in Supporting Information S1.

The tidal ellipses of the four dominant constituents are shown in Figure 7. The semidiurnal tides have larger maximum speeds than the diurnal tides, as indicated by the values of the respective semi-major axes (see Table 3). The ellipses of the four dominant constituents are oriented broadly north-south, which is nearly parallel to the coastline of Berkner Island. The diurnal tides are relatively depth-independent and nearly rectilinear, as indicated

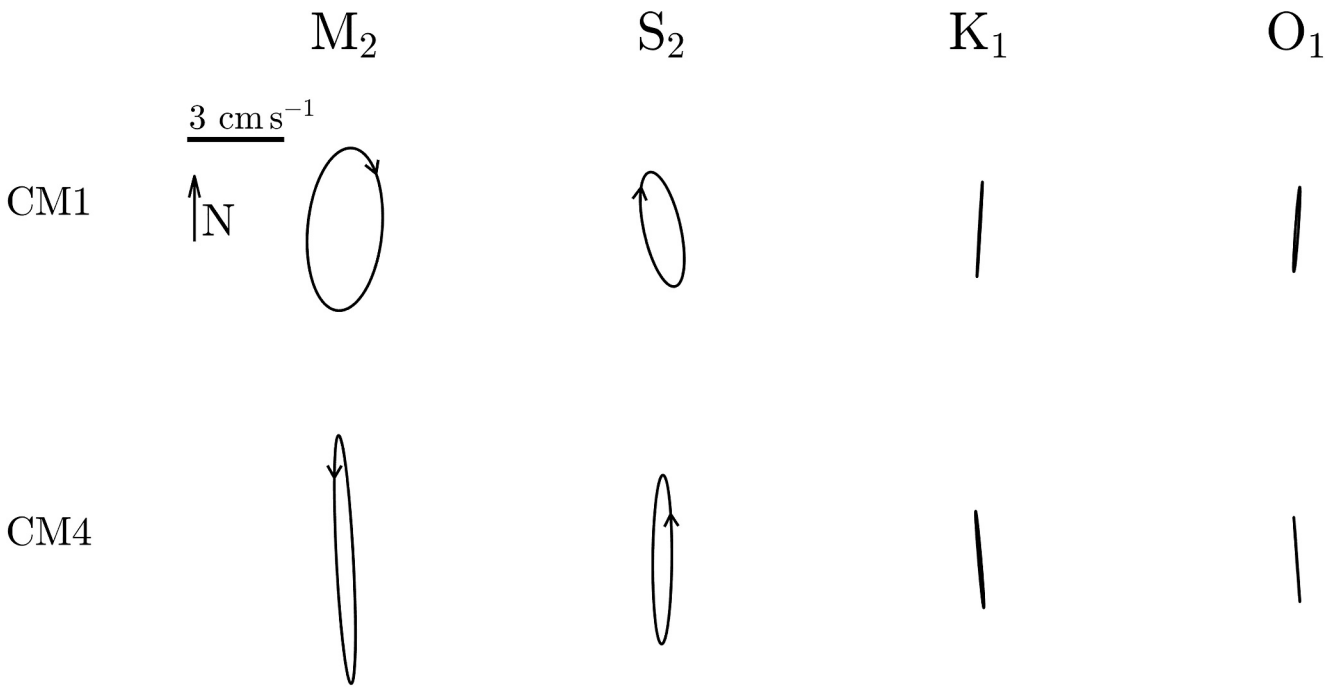


**Figure 7.** Tidal ellipses for the four dominant tidal constituents ($M_2$, $S_2$, $K_1$, $O_1$) obtained from harmonic analysis spanning the full 3-year time series at the upper current meter (CM) (CM1, top row) and at the lower CM (CM4, bottom row), with the arrow heads indicating the sense of direction of the nondegenerate ellipses. The ellipse parameters are listed in Table 3. The vertical arrow labeled "N" indicates True North.

by a near zero polarization at both CM1 and CM4. The semidiurnal tides at CM4 are also close to rectilinear. However, for those two constituents, the tidal current vector at CM1 traces a more distinct elliptical shape compared with deeper in the water column, and the semi-major axes of the ellipse is reduced near the ice base. These depth-dependent features, as well as their potential variability throughout the observational period, will be examined in detail in Section 5.

In addition to providing insights into the dominant tidal constituents, the harmonic analysis also indicates that tides account for nearly 50% of the variance at CM4 (compared with 90% at Site 3, as reported by Jenkins et al. (2010)). The time series of the 36-hr low-pass filtered tidal current magnitude at CM1 and CM4 (blue curves in Figures 6a and 6b) reveal a clear fortnightly signal, which will be explored further in Section 3.4.

### 3.3. Basal Melt Rates

Building on the characterization of the water column structure and local dynamics presented above, we now describe the key features of the melt rate record.

The ApRES-derived melt rate time series (purple curve in Figure 6c) displays strong high-frequency variability with values ranging between ∼0.1 m $yr^{-1}$ and ∼3.0 m $yr^{-1}$, and a mean of 1.1 m $yr^{-1}$ over the 1-year observation period. As detailed in Section 2.3, the year-long ApRES record was extended using the basal melt rate parameterization of Jenkins et al. (2010) with optimized parameters. The resulting 36-hr low-pass filtered parameterized melt rate time series (gray curve in Figure 6c) shows a similar level of variability and yields a mean melt rate of 1.2 m $yr^{-1}$ over the 3-year period, with yearly means of 1.1, 1.0, and 1.5 m $yr^{-1}$ in 2015, 2016, and 2017, respectively.

The ApRES-derived melt rates correlate strongly with the 36-hr low-pass filtered current magnitude at CM1 during 2015 ($r = 0.82$). A similarly strong relationship is found with the current magnitude at the deeper CM located approximately 155 m below the ice base ($r = 0.76$), consistent with the vertically coherent flow described in Section 3.2. When considering lower frequency variability, the correlation strengthens further: the 30-day low-pass filtered melt rates correlate with the current magnitude at CM1 and CM4 at $r = 0.94$ and $r = 0.92$, respectively.

**Table 3**
*Ellipse Parameters (Semi-Major Axis a, Semi-Minor Axis b, Inclination Ψ, Phase Φ) Associated With the Tidal Constituent Ellipses Shown in Figure 7*

| Mooring sensor | Tidal constituent | Frequency (cpd) | Critical latitude | $a$(cm s$^{-1}$) | $b$(cm s$^{-1}$) | Ψ(°) | Φ(°) |
|---|---|---|---|---|---|---|---|
| CM1 (at 679 m) | $M_2$ | 1.93 | ≈74°S | 3.36 ± 0.13 | −1.54 ± 0.11 | 85 ± 3 | 316 ± 4 |
| | $S_2$ | 2.00 | ≈85°S | 2.41 ± 0.14 | −0.76 ± 0.12 | 103 ± 4 | 39 ± 4 |
| | $K_1$ | 1.01 | ≈30°S | 1.96 ± 0.08 | −0.02 ± 0.11 | 87 ± 3 | 251 ± 2 |
| | $O_1$ | 0.93 | ≈27°S | 1.75 ± 0.07 | −0.06 ± 0.08 | 86 ± 3 | 192 ± 3 |
| CM4 (at 815 m) | $M_2$ | 1.93 | ≈74°S | 5.12 ± 0.14 | 0.35 ± 0.06 | 93 ± 1 | 311 ± 1 |
| | $S_2$ | 2.00 | ≈85°S | 3.48 ± 0.15 | 0.39 ± 0.05 | 90 ± 1 | 58 ± 2 |
| | $K_1$ | 1.01 | ≈30°S | 2.00 ± 0.08 | 0.05 ± 0.07 | 95 ± 2 | 248 ± 2 |
| | $O_1$ | 0.93 | ≈27°S | 1.74 ± 0.09 | 0.01 ± 0.08 | 94 ± 2 | 190 ± 3 |

*Note.* Inclination angles are defined positive anticlockwise from due east (Foreman, 1978). Parameter values are presented as the mean ±95% confidence intervals.

The ApRES-derived basal melt rate signal also correlates strongly with temperatures at the upper two CT sensors ($r = 0.93$ at CT1 and $r = 0.89$ at CT2 when considering 30-day low-pass filtered time series), both located within the Berkner-sourced HSSW part of the water column (Figure 3). In contrast, there is no correlation between the ApRES melt rate and the temperature at the two deepest sensors, CT5 and CT6, which sample the Ronne-sourced portion of the water column (Figure 3). This supports the conclusion by Vaňková and Nicholls (2022) that seasonal basal melt rate variability at Site 5c is primarily driven by variability in the Berkner-sourced layer of the water column rather than being influenced by variations in the inflow of Ronne-sourced HSSW. The potential link between seasonal variations in upper water column temperatures and melt rates can also be observed by comparing the 30-day low-pass filtered melt rate with the −2.27°C contour in Figure 4a: when the upper water column cools, as indicated by a deepening of the isopycnal (e.g., between June 2015 and January 2016) the melt rate decreases, and conversely, when the isopycnal shoals (e.g., between January 2016 and April 2016) melt rate increases.

### 3.4. Spring-Neap and Tidal Variability

Sections 3.1-3.3 have mostly focused on characterizing the mean state and seasonal variability over the 3-year observational period. To investigate temporal variability on timescales shorter than 30 days, we compute the power spectral density (PSD) of the ApRES-derived basal melt rate time series and of the ocean properties time series measured at the upper and lower CM/CT instrument clusters (CM1/CT1 and CM4/CT4, respectively), shown in Figure 8.

The PSD of the two current magnitude time series (red curves in Figures 8a and 8b) reveal a mixed tidal signal with strong diurnal and semidiurnal tides. Within the diurnal and semidiurnal bands, the dominant peaks appear at the $O_1$, $K_1$, $M_2$, and $S_2$ tidal frequencies (in line with the results from the harmonic analysis presented in Section 3.2). As expected from the orientation of the velocity components with respect to the coast of Berkner Island (north-south component $v$ nearly coast-parallel), the amplitude of the dominant peaks is larger in the $v$ than in the $u$ component spectra. This is particularly apparent at $O_1$ and $K_1$, and consistent with the previously described degenerate diurnal tidal ellipses (Figure 7). Around the $M_2$ and $S_2$ spectral peaks at CM1, some of the energy appears smeared to lower and higher frequencies, forming a "tidal cusp" (Munk et al., 1965). The presence of a semidiurnal tidal cusp suggests that the $M_2$ and $S_2$ tides are losing energy through nonlinear interaction with the slowly varying background flow or via quadratic boundary friction at the ice shelf-ocean interface (Munk & Cartwright, 1966), as explored further in Section 5.1.

In Section 3.2, we noted that the estimated tidal current magnitude features strong fortnightly variability (blue curves in Figures 6a and 6b), suggesting the presence of a spring-neap tidal cycle. Spring-neap tidal variability in current magnitude arises from nonlinear interactions between the semidiurnal constituents $M_2$ and $S_2$, or between the diurnal constituents $O_1$ and $K_1$. The difference between the $S_2$ and $M_2$ tidal frequencies produces a compound tide with the same frequency as the lunar synodic fortnightly tidal constituent $M_{sf}$ (0.068 cpd; equivalent to a period of 14.77 days). Similarly, the difference between the $O_1$ and $K_1$ tidal frequencies generates a signal with

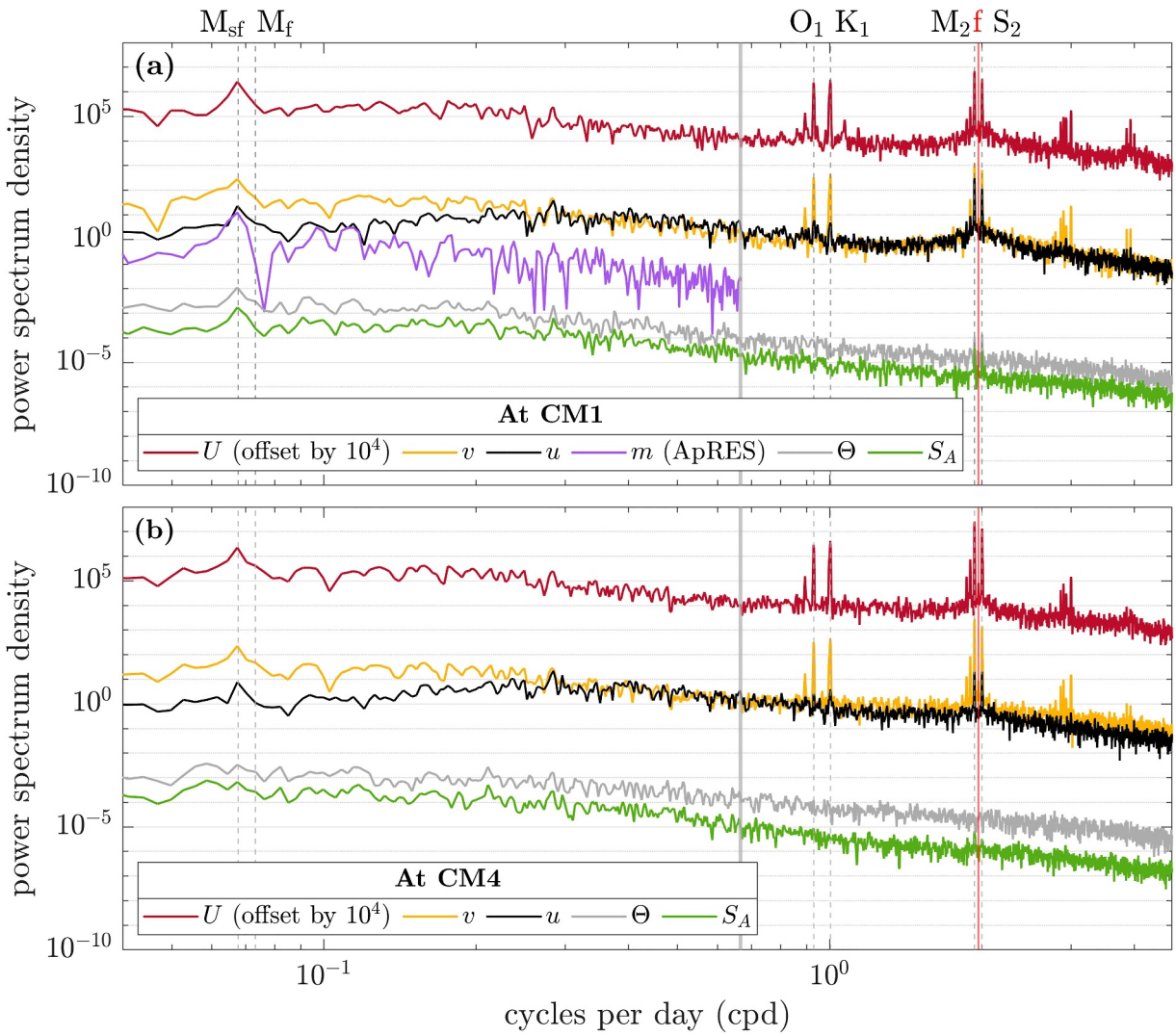


**Figure 8.** Power spectral density of the ApRES-derived basal melt rates, velocity components $v$ and $u$, current speed $U$, temperature $\Theta$, and salinity $S_A$. The $U$ spectra (red curves) have been offset by a factor of $10^4$ to improve readability. The ocean property spectra are computed using data from the upper mooring sensors CM1 and CT1 located at 679 m below sea level (a), and from data from CM4 and CT4 located at 815 m below sea level (b). All spectra were computed using Welch's method, 50% overlapping. The vertical dashed gray lines indicate, from left to right, the fortnightly tidal frequencies $M_{sf}$ (0.068 cpd) and $M_f$ (0.073 cpd), the diurnal tidal frequencies $O_1$ (0.93 cpd) and $K_1$ (1.01 cpd), and the semidiurnal tidal frequencies $M_2$ (1.93 cpd), and $S_2$ (2.00 cpd). The vertical red line indicates the Coriolis frequency $f$ at the Site 5c latitude (1.97 cpd). The solid gray line indicates the low-pass filter cutoff frequency (36 hr; 0.67 cpd) applied when processing the ApRES data to derive basal melt rates (see Section 2.2.2).

the same frequency as the lunar fortnightly tidal constituent $M_f$ (0.073 cpd; equivalent to a period of 13.66 days). The current magnitude spectra feature a peak at $M_{sf}$ (and no peak at $M_f$), indicating that the observed fortnightly signal at Site 5c is caused by interaction between the two dominant semidiurnal constituents.

In contrast to the velocity spectra, which feature a dominant level of variability at tidal (≥1 cpd) frequencies, the PSD of the temperature and salinity time series (gray and green curves, respectively) feature a dominant level of variability at lower frequencies. In the scalar spectra of the CT1 records, this is emphasized by the presence of a dominant peak at $M_{sf}$ and less pronounced, lower amplitude peaks at $M_2$ and $S_2$. The semidiurnal spectral peaks do not appear in the PSD calculated from the CT4 time series, and they are also absent in the diurnal frequency range at both depths. A possible explanation for the observed semidiurnal variability in temperature and salinity at the upper instrument is vertical strain due to internal tidal waves. This would imply water column heave, which is consistent with the more pronounced variability in the individual temperature profiles at CT1 compared with CT4 (gray curves in Figure 2). However, water column heave would be expected to induce cross-isopycnal density

changes in $\Theta - S_A$ space, which can not be clearly detected at CT1. Another potential explanation is tide-induced turbulent mixing in the sub-ice shelf boundary layer, with the absence of diurnal variability explained by critical latitude effects. This mechanism will be discussed further in Section 5.1.

For reasons explained in Section 2.2.2, the ApRES-derived basal melt rate time series was low-pass filtered with a 36-hr cutoff, restricting the power spectrum analysis to frequencies lower than 0.67 cpd (indicated by the solid vertical gray line in Figure 8) for this signal. The fortnightly spring-neap signal observed in the velocity and scalar time series also appears in the ApRES-derived basal melt rate PSD (purple curve in 8a). The presence of $M_{sf}$ spectral peaks in current speed, temperature, and salinity indicates that basal melting spring-neap variability could be driven by spring-neap variations in flow and/or thermal driving. The drivers of basal melt rate variability across multiple time scales, including spring-neap, are explored in more detail in the next section.

To visualize the spring-neap variability associated with the $M_{sf}$ peak identified in the power spectra of the near-ice current magnitude, temperature, and melt rate, we construct spring-neap composites of $U$ at CM1, $\Theta$ at CM1, and $m$ derived from the ApRES measurements (Figure 9). The first year of the record is divided into 14.76-day segments (yielding 24 segments), and the composites are calculated by averaging each hourly time point across all segments. Consistent with Figure 8, the near-ice current magnitude, near-ice temperature, and melt rate all display visible fortnightly variability, with neap-to-spring ranges of 3.6 cm $s^{-1}$, 0.02°C, and 0.6 m $yr^{-1}$, respectively. When expressed relative to the composite mean, these ranges correspond to variations of approximately ±17%, ±0.5%, and ±26% around the mean for the current magnitude, temperature, and melt rate, respectively. Although not shown here, the percentage variation in thermal driving relative to its spring-neap composite mean is approximately ±13%. Although this is smaller than the ±17% variation observed in current speed, it is still substantial, suggesting that the observed melt rate spring-neap variability is driven by variations in both current magnitude and thermal driving. We examine the drivers of basal melt rate variability in more detail in the next section.

## 4. Drivers of Basal Melt Rate Variability

To identify the dominant drivers of basal melt rate variability, we perform a dynamical-thermodynamical decomposition based on near-ice base oceanographic measurements. This approach is analogous to that used by Jourdain et al. (2019) and Richter et al. (2022) to identify the dominant drivers of tide-driven basal melting from numerical simulation outputs.

The strong agreement between ApRES-derived melt rates and melt rates predicted using the three-equation formulation with constant coefficients (Figure A1) suggests that the ice shelf-ocean boundary layer at Site 5c is predominantly shear-driven and weakly stratified. Under such conditions, basal melt rate is expected to scale linearly with the product of friction velocity and thermal driving (Vreugdenhil & Taylor, 2019). Consistent with this, we find that the product of current magnitude at CM1 and thermal driving at CT1 explains $r^2 = 88\%$ of the variability in the ApRES-derived melt rate record. This implies that the following relationship holds at Site 5c:

$$m \propto U\, T_* \,, \tag{5}$$

where $U$ corresponds to the current magnitude measured at CM1, and $T_*$ is the thermal driving calculated as $T - \left(\lambda_1\, S + \lambda_2 + \lambda_3\, p_b\right)$ using temperature and salinity measured at CT1. To evaluate the portion of the melt rate induced by temporal variations above a given frequency, we can decompose $U$ and $T_*$ into a slowly varying component and a rapidly varying component, that is, $U = U^{lp} + U'$ and $T_* = T_*^{lp} + T_*'$, with the superscript $lp$ designating the slow variations and primes denoting the fast variations. The slowly varying components ($U^{lp}$ and $T_*^{lp}$) are obtained by applying a low-pass filter to the observed time series and the rapidly varying components ($U'$ and $T'$) are then calculated by subtracting the derived slowly varying component from the observed time series. The right-hand side of Equation 5 can then be expressed as the linear sum of four terms:

$$m \propto U^{lp}\, T_*^{lp} + U^{lp}\, T_*' + U'\, T_*^{lp} + U'\, T_*' \,, \tag{6}$$

with the first term on the right-hand side corresponding to the mean term and the last three terms corresponding to the fluctuating terms. Following Jourdain et al. (2019) and Richter et al. (2022), we refer to these last three terms

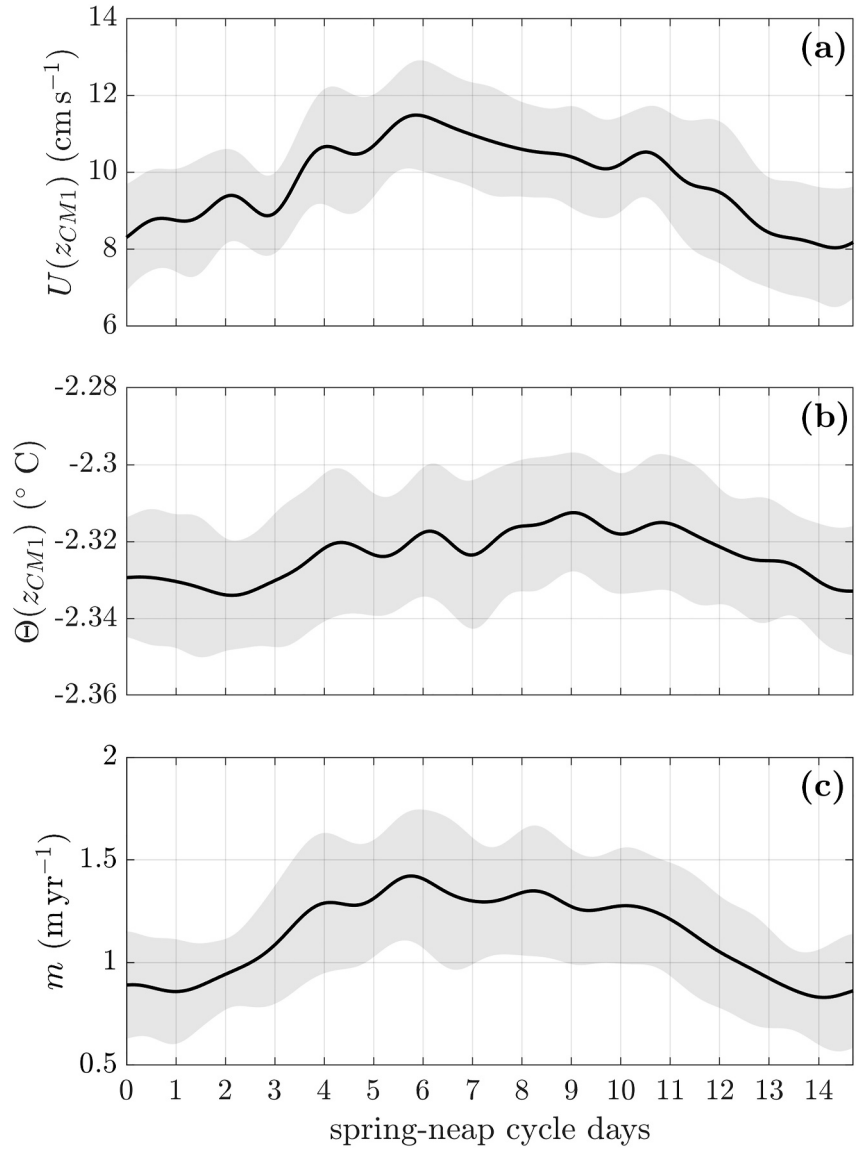


**Figure 9.** Spring-neap cycle composites of 36-hr low-pass filtered (a) current speed at CM1; (b) temperature at CM1; (c) ApRES-derived melt rate. The composites are constructed from 24 spring-neap cycles. Shading shows one standard deviation around the composites.

as the thermodynamical ($U^{lp}\ T'_*$), dynamical ($U'\ T^{lp}_*$), and covariational ($U'\ T'_*$) terms, respectively. The drivers of basal melt rate variability on a given time scale can then be quantified based on the relative contribution of the fluctuating terms to the variance of their sum for a given low-pass cutoff frequency.

Figure 10 presents the standard deviation of the dynamical, thermodynamical and covariational terms (colored curves), as well as the standard deviation of their sum (black solid curve) for low-pass filter cutoff values capturing tidal to seasonal timescales. The sum of the standard deviations of each term is also shown (black dashed curve) to highlight that the three terms are correlated, which explains why their variances do not add up to the variance of their sum (if the terms were independent the black solid and dashed lines would coincide). Note that the full 3-year records of $U$ and $T_*$ were used for this analysis.

To evaluate tide-induced basal melt rate drivers, we consider a cutoff frequency of 36 hr (0.67 cpd), which, based on the spectral analysis presented earlier (Figure 8a), should effectively separate the high-frequency variability associated with mixed diurnal/semidiurnal tides at Site 5c. Although there may be other sources of high frequency

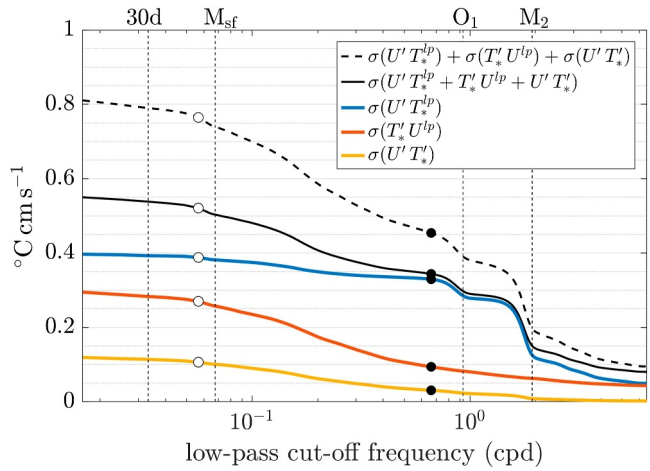


**Figure 10.** Evaluation of drivers of melt rate variability based on ocean data collected at the upper instrument cluster (CM1/CT1). The curves correspond to the standard deviation of each of the last three terms on the right-hand side of Equation 6 (color-coded), to the standard deviation of their sum (black solid) and to the sum of their standard deviations (black dashed). The black and white markers indicate low-pass filter cutoff values of 36 hr (0.67 cpd) and 17 days (0.06 cpd), respectively.

variability in addition to tides, we assume for the purpose of this analysis that the variability on timescales shorter than 36 hr is dominated by tides, as suggested by the peaks of energy to the right of the vertical gray line in Figure 8a. As indicated by the black markers in Figure 10, when considering a 36 hr cutoff frequency, the dynamical term ($U'\ \Theta'^{lp}_*$) dominates, with a smaller, but not insignificant, contribution from the thermodynamical term ($U^{lp}\ \Theta'_*$). This suggests that enhanced near-ice base current speed and associated enhanced shear-driven turbulent mixing is the dominant mechanism driving basal melt rate variations on tidal timescales, with a smaller contribution from tide-induced changes in thermal driving.

As the timescales of variability increases, the relative contribution of the terms including $T'_*$ also increases. As shown by the white markers in Figure 10, when considering variability on spring-neap time scales and longer, the thermodynamical term becomes nearly as important as the dynamical term, indicating a greater effect of temperature variance on melt rate variability. In Section 3.4, we hypothesized that the tidal and spring-neap signals observed in the temperature power spectrum arise from tide-induced turbulent mixing entraining warmer water into the mixed layer. The growing contribution of the thermodynamical term at longer timescales may therefore reflect an increased role of this process in modulating the heat available for melting. Nevertheless, even at these longer timescales, the dynamical term remains the largest contributor, indicating that variability in current speed continues to be the dominant driver of melt rate variability.

## 5. Tidal Current Vertical Structure

Having established that tidal variability, particularly in near-ice base current speed, is a primary driver of high-frequency basal melt rate variability at Site 5c, we now investigate vertical structure of these tidal currents. Understanding how friction at the ice base influences the tides is essential for accurately parameterizing basal melt rates in tidal environments. Within the constraints of a mooring design equipped with only two CMs, we utilize the velocity measurements at CM1 and CM4 to assess changes in tidal current characteristics between the middle of the water column and the near-ice base region at Site 5c. A modeling study by Makinson (2002) showed that tidal vertical mixing and associated basal melting depend not only on the mean magnitude of the tidal current but also on tidal ellipse polarization. We therefore examine both the magnitude and the rotational properties of the tidal current.

### 5.1. Depth-Dependence of the Tidal Ellipse Properties

#### 5.1.1. Mean State

In Section 3.2 we noted that the tidal ellipses of the diurnal constituents $O_1$ and $K_1$ remain relatively unchanged between CM1 and CM4, whereas the $M_2$ and $S_2$ tidal ellipses are more circular with a clockwise (CW) rotation at

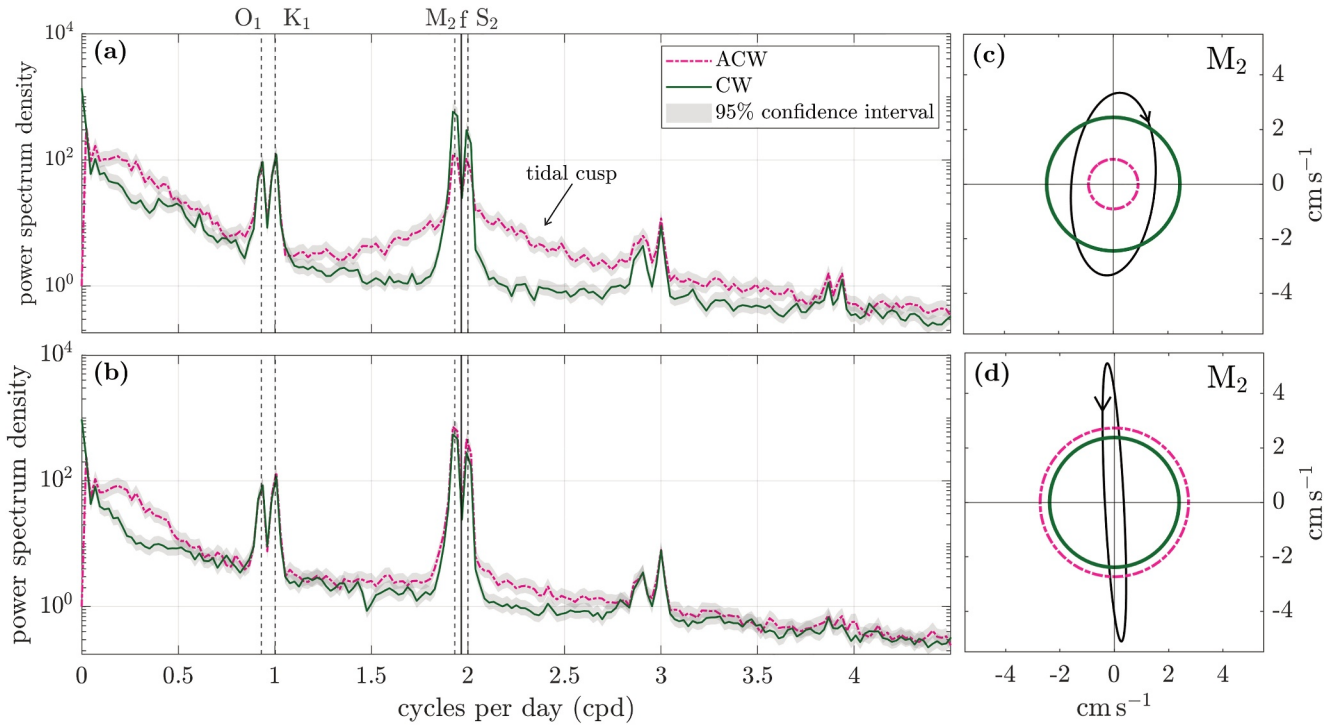


**Figure 11.** (a, b) Power spectra of the anti-clockwise (ACW) (pink dashed) and clockwise (CW) (green solid) rotary components time series at CM1 (a) and CM4 (b), computed using Welch's method, 50% overlapping. (c, d) Decomposition of the $M_2$ tidal ellipse at CM1 (c) and CM4 (d) into its ACW (pink dashed) and CW (green solid) rotary components. Note that the tidal ellipses in (c, d) correspond to the $M_2$ ellipses shown in Figure 7.

CM1, located close to the ice shelf base (Figure 7). In order to interpret these observed changes of the tidal ellipses with depth, and following the approach taken by previous studies of tides underneath and near Ronne Ice Shelf (Foldvik et al., 2001; Makinson, 2002; Makinson et al., 2006), we decompose the velocity vector of each of the dominant tidal constituents into their respective CW and anti-clockwise (ACW) rotary components. As described in Text S1 in Supplemental Information S1, the semi-major and semi-minor axes of the tidal ellipse of any tidal constituent can be expressed in terms of the ACW and CW rotary component magnitudes $R_{+/-}$ (Gonella, 1972; Prandle, 1982):

$$a = R_+ + R_- \,, \tag{7}$$

$$b = R_+ - R_- \,. \tag{8}$$

It follows that the tidal ellipse polarization can be described as follows:

$$P = \frac{b}{a} = \frac{R_+ - R_-}{R_+ + R_-} \,, \tag{9}$$

implying that any changes in shape of the tidal ellipse with depth corresponds to a change in the relative size of the two rotary components with depth. Moreover, Equation 9 highlights that when the rotary components have equal magnitude ($R_+ = R_-$), the tidal velocity vector traces out a flat ellipse ($P = 0$), indicating rectilinear tidal flow. Conversely, when the magnitude of either of the two rotary components is equal to zero, the corresponding tidal ellipse is circular with either an ACW ($R_- = 0; P = +1$) or a CW ($R_+ = 0; P = 1$) sense of rotation.

Figures 11a and 11b shows the PSD of the rotary component time series at CM1 and CM4. Within the range of frequencies shown in this plot (0–4.5 cpd), we are particularly interested in the frequency bands of the dominant diurnal and semidiurnal tidal constituents. Consistent with the earlier description of the tidal ellipses, this figure shows that in the diurnal frequency band, the ACW and CW components have spectral peaks of very similar

amplitude, translating into rectilinear tides, at both depths (Figures 11a and 11b). In the semidiurnal frequency band, however, the ACW and CW component peaks have a similar amplitude at CM4, but different amplitudes at CM1, where the ACW component is reduced (Figures 11a and 11b). This shows that the change in the shape of the semidiurnal tidal ellipses, from near-rectilinear at CM4 (as shown in Figure 11d for $M_2$) to more circular at CM1 (as shown in Figure 11c for $M_2$), is caused by a reduction of the energy in the ACW component at CM1 compared with CM4. Moreover, the tidal cusp noted in the velocity components PSD (Figure 8) appears only in the ACW PSD at CM1, suggesting that the nonlinear mechanism causing the loss of energy is associated only with the ACW component, and only takes place near the ice base.

#### 5.1.2. Inferred Mean Vertical Profiles of the Rotary Components

The vertical variations of the mean rotary properties of the tidal current described above can be explained in terms of the varying distances from the ice shelf base over which the ACW and CW rotary components are influenced by boundary friction (Prandle, 1982; Soulsby, 1983). We first provide a derivation of these length scales, before showing that the observed 3-year mean vertical structure of the dominant tides at Site 5c are consistent with this model.

In order to describe a tidal oscillation on the rotating Earth, two independent equations of motion, one for the ACW (+) and one for the CW (−) component of the flow can be derived for a given tidal constituent of angular frequency $\omega$ (see Text S2 in Supplemental Information S1 for the derivation):

$$i\,(\omega + f)\,\widetilde{R_+} = -\widetilde{p_+} + \frac{\partial}{\partial z}\left(\nu\,\frac{\partial}{\partial z}\,\widetilde{R_+}\right), \tag{10}$$

$$-i\,(\omega - f)\,\widetilde{R_-} = -\widetilde{p_-} + \frac{\partial}{\partial z}\left(\nu\,\frac{\partial}{\partial z}\,\widetilde{R_-}\right), \tag{11}$$

where $i = \sqrt{-1}$, $f$ is the Coriolis frequency, $\nu$ is the eddy viscosity, $\tilde{R}_{+/-}$ are the two counter-rotating velocity phasors, and $\tilde{p}_{+/-}$ are the two counter-rotating pressure gradient phasors. Based on dimensional analysis of the terms on the left-hand side of Equations 10 and 11, we can formulate the following characteristic time scales for the ACW and CW components, respectively:

$$\tau_{+/-} \sim \frac{1}{|\omega \pm f|}\,. \tag{12}$$

By definition, the viscous timescale, that is, the timescale required by viscosity $\nu$ to diffuse momentum a distance $\delta$ from the boundary, is defined as:

$$\tau_\nu \sim \frac{\delta^2}{\nu}\,. \tag{13}$$

The length scales $\delta_{+/-}$ over which the effects of viscosity influence the ACW and CW components can hence be derived from $\tau_{+/-} \sim \tau_\nu$, yielding:

$$\delta_{+/-} = \left(\frac{\nu}{|\omega \pm f|}\right)^{1/2}. \tag{14}$$

It is worth noting that $\delta_+$ and $\delta_-$, which are defined for individual tidal constituents, are often referred to in the literature as "tidal boundary layers." This reflects the view that the boundary layer can be defined as the maximum depth at which the presence of the boundary is felt at any timescale. In this paper, however, we define the frictional boundary layer as that which is relevant to the three-equation melt rate formulation, namely, the region beyond which the total flow (resulting from the combined influence of all tidal constituents and any nontidal accelerations) can be assumed to have reached free-stream. Therefore, rather than referring to $\delta_+$ and $\delta_-$ as tidal boundary layer thicknesses, we instead refer to them here as viscous length scales associated with the ACW and CW rotary components, respectively. According to Equation 14, in the Southern Hemisphere (where $f$ is

negative), $\delta_+ > \delta_-$, implying that the ACW component feels the effect of boundary friction up to a larger distance from the ice base than the CW component. The difference between $\delta_+$ and $\delta_-$ increases with proximity to the critical latitude, as quantified by the ratio:

$$\frac{\delta_+}{\delta_-} = \left(\frac{|\omega - f|}{|\omega + f|}\right)^{1/2}, \tag{15}$$

At Site 5c, located near the semidiurnal critical latitudes and further away from the diurnal critical latitudes (Table 3), $\delta_+/\delta_- \sim 11$ for the semidiurnal tides and $\sim 2$ for the diurnal tides. Assuming a water column with vertically uniform eddy viscosity, and setting the boundary condition $R_{+/-} = 0$ at the ice base, Equations 10 and 11 are satisfied by the solution:

$$R_{+/-}(z) = R^{\infty}_{+/-}\left(1 - e^{-C\, z/\delta_{+/-}}\right), \tag{16}$$

with $z$ the distance from the ice base, $R^{\infty}_{+/-}$ the free-stream magnitude (with $R^{\infty}_{+} = R^{\infty}_{-}$ in the case of a rectilinear free-stream flow), and $C$ a constant used to define $\delta_{+/-}$ based on the number of e-folding scales it corresponds to. In this paper, we follow Soulsby (1983) in choosing $C = 2$, which gives $R(\delta) = 0.9\, R^{\infty}$. It is worth noting that while the chosen value of $C$ influences the values of $\delta_+$ and $\delta_-$, it does not influence the inferred profiles.

We now show that the mean rotary properties of the dominant tidal constituents, observed at CM1 and CM4, are relatively consistent with the $R_{+/-}$ vertical profiles predicted by Equation 16, despite the approximation of a depth-independent eddy viscosity. To do so, we need estimates for $\delta_{+/-}$ and $R^{\infty}_{+/-}$. We start by using the observed values of $R_+$ at CM1 and CM4 to solve for $\delta_+$ from:

$$\frac{R_+(z_{CM1})}{R_+(z_{CM4})} = \frac{1 - e^{-2\, z_{CM1}/\delta_+}}{1 - e^{-2\, z_{CM4}/\delta_+}}, \tag{17}$$

with $z_{CM1}$ and $z_{CM4}$ the distance of CM1 and CM4 from the ice base (Table 1). Using the inferred value of $\delta_+$, we calculate $\delta_-$ from Equation 15. We then use the estimated values of $\delta_+$ and $\delta_-$ in combination with the observed values of $R_+$ and $R_-$ at CM1 to obtain $R^{\infty}_{+}$ and $R^{\infty}_{-}$ from Equation 16. This procedure constrains the $R_+$ and $R_-$ profiles to pass through zero at the ice base, through the observed values of $R_+$ and $R_-$ at CM1, and through the observed value of $R_+$ at CM4. The procedure does not use the observed value of $R_-$ at CM4. Hence, the level to which the observations agree with the theoretical model can be assessed based on the difference between the observed and predicted values of $R_-$ at CM4.

The resulting profiles, shown in Figure 12, are consistent with the observed rotary component magnitudes. Note that the profiles only account for boundary effects at the ice base, neglecting any frictional effects at the seafloor. Comparing the pink and green shading in Figures 12a and 12b highlights that, in the case of $M_2$ and $S_2$, $\delta_- < z_{CM1} < \delta_+$. This implies that for the two dominant semidiurnal constituents, the ACW rotary component magnitude ($R_+$) is influenced by boundary friction at CM1, whereas the CW rotary component is unaffected by boundary friction at the same depth (as observed in Figure 11 for $M_2$). As a result, there is a pronounced reduction in $R_+$ and nearly no difference in $R_-$ at CM1 relative to the free-stream. Given that the free-stream flow is close to rectilinear (expected from the proximity of the site to the coast of Berkner Island), this results in an ACW sense of rotation ($R_- > R_+$) at CM1.

Furthermore, comparing the profiles predicted for the semidiurnal constituents (Figures 12a and 12b) with those predicted for the diurnal constituents (Figures 12c and 12d) highlights the effect of proximity to the critical latitude on the distance from the ice base over which $R_+$ is affected by viscosity: because of the much smaller $\delta_+$ for diurnal compared with semidiurnal tides at Site 5c (Equation 14), $R_+$ reaches its free-stream value much closer to the ice base at $K_1$ and $O_1$ frequencies compared with $M_2$ and $S_2$. Based on the assumed value of $C$, the calculated $\delta_+$ for the diurnal constituents is smaller than the distance between the ice base and CM1. This is in line with the observed rectilinear diurnal tidal ellipses at both CM1 and CM4 (Figure 7). Furthermore, the difference between the $R_+$ and $R_-$ profiles is much smaller in the case of the diurnal constituents compared with the semidiurnal constituents, as expected from the much smaller ratio $\delta_+/\delta_-$ for diurnal compared with semidiurnal tides at Site 5c (Equation 15).

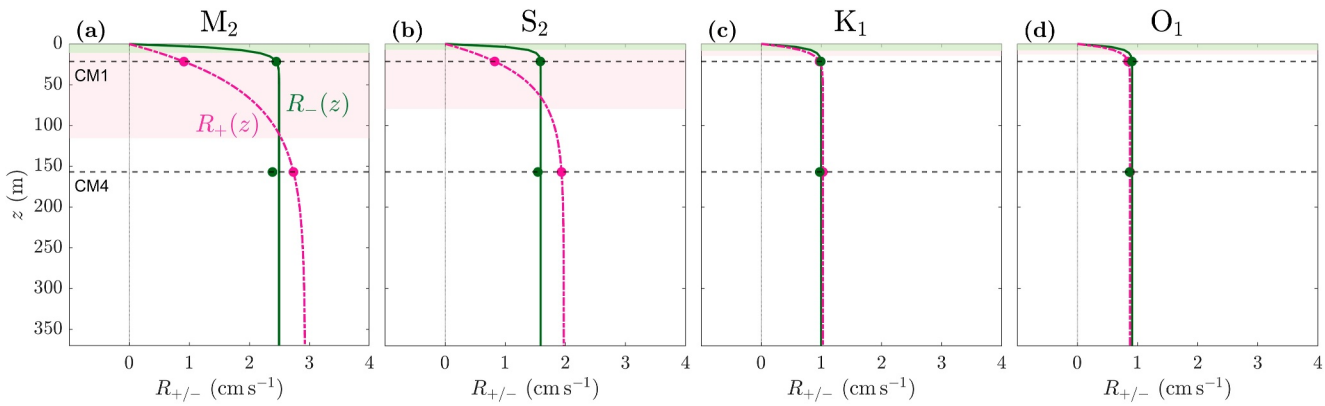


**Figure 12.** Vertical profiles of the anti-clockwise (ACW) rotary component ($R_+(z)$; pink dashed) and clockwise (CW) rotary component ($R_-(z)$; green solid) predicted from Equation 16 for the dominant semidiurnal (a, b) and diurnal (c, d) tidal constituents. The markers correspond to the values of $R_+$ and $R_-$ derived from the current measurements at CM1 and CM4. The shading indicates the estimated viscous length scales of the ACW component ($\delta_+$; pink shading) and of the CW component ($\delta_-$; green shading).

The quantitative interpretation of the vertical variations of $R_+$ and $R_-$ agrees with the qualitative features of the power spectra in Figure 11. Thus, the theoretical considerations described above are able to explain all of the tidal constituent ellipse vertical variations shown in Figures 7 and 11.

### 5.1.3. Temporal Variability

The tidal ellipse characteristics presented in Figures 11 and 12 represent a mean state over the 3-year mooring record. Over this same period, however, the viscosity profile, and subsequently the tidal current profiles, may change. To examine the possible temporal variability of the tidal ellipse characteristics, and assess if the depth-independent viscosity assumption holds throughout the record, we perform a harmonic analysis over 27.6-day-long sections rather than over the full CM records. The minimum window length applied for this analysis is limited by the period of data required to differentiate tidal constituents of close frequencies, as determined from the Rayleigh criterion (Godin, 1972). In order to maximize the window length while maintaining accuracy, we only include the six dominant tidal constituents ($M_2$, $S_2$, $N_2$, $K_1$, $O_1$, $Q_1$) in this analysis. Limiting the harmonic analysis to these six constituents only reduces the variance explained by tides from 49% to 46% at CM4. Starting with the initial 27.6-day section of the CM1 and CM4 records and then moving the 27.6-day window forward in 1-day increments until the end of the records is reached, yields time series of tidal ellipse properties at CM1 and CM4.

Figure 13a presents the resulting time series of low-frequency variations of the $M_2$ tidal ellipse polarization at CM1 and CM4. At CM4, the polarization is near zero throughout the 3-year period, indicating that the tidal flow remains nearly rectilinear throughout the record, as noted in the mean state analysis. At CM1 however, the polarization deviates from the 3-year mean polarization of $P = -0.46$, with variations between $P = -1$ (CW circular ellipse) and $P = 0$ (rectilinear flow). As shown in Figure 13b, the low-frequency variations in $P$ at CM1 are driven by changes in the ACW rotary component magnitude $R_+$ (solid pink curve).

Similar low-frequency changes in tidal ellipse polarization in the bottom boundary layer have been described by Makinson et al. (2006) based on observations from open ocean moorings near Ronne Ice Front, and attributed to seasonal changes in stratification caused by HSSW production during sea ice formation periods. Given the minimal density structure variability at Site 5c (Figure 5) compared with the pronounced seasonal variations closer to the sea ice production sites, changes in stratification are not likely to induce the changes in polarization observed here. Instead, at Site 5c, the variations in the near-ice base tidal ellipse polarization appear to correlate with nontidal background flow variations at the same depth (red curve in Figure 13a), with a more circular tidal ellipse ($P \rightarrow -1$) at CM1 during periods of higher flow. Changes in flow speed are expected to change the eddy viscosity, in turn modifying the distance over which boundary friction influences the rotary components (Equation 14).

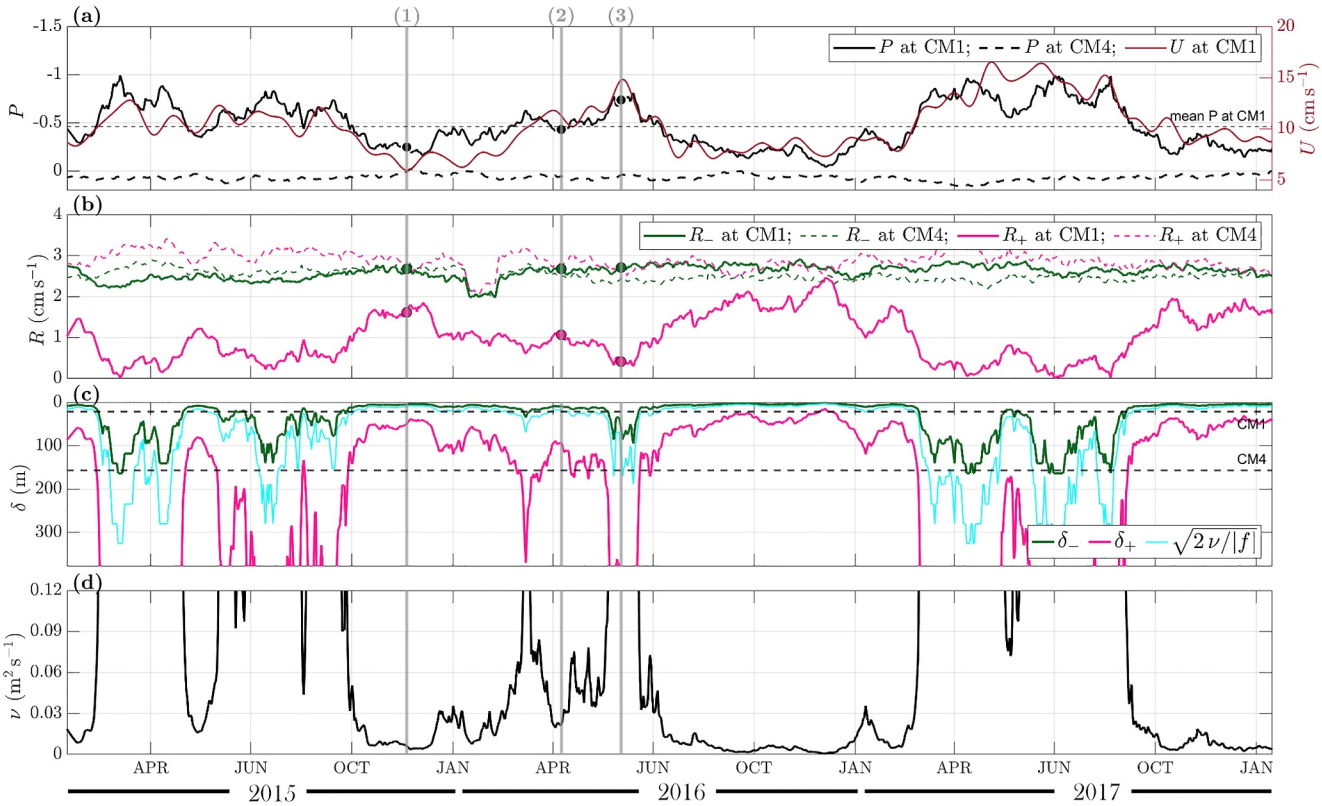


**Figure 13.** Temporal variation of the $M_2$ tidal current characteristics and inferred viscous length scales and viscosity: (a) tidal ellipse polarization $P$ at CM1 (black solid curve; with the 3-year mean indicated by the horizontal dashed line) and at CM4 (black dashed curve), and observed 30-day low-pass filtered current magnitude at CM1 (red curve); (b) magnitude of the clockwise (CW) rotary component ($R_-$, green) and of the anti-clockwise (ACW) rotary component ($R_+$, pink) at CM1; (c) estimated viscous length scales associated with the CW rotary component ($\delta_-$, green) and the ACW rotary component ($\delta_+$, pink), and Ekman depth calculated as $\sqrt{2\nu/|f|}$ (cyan), with the horizontal dashed lines indicating the position of CM1 and CM4 in the water column; (d) eddy viscosity estimated from Equation 14 using the $\delta_+$ time series shown in (c). The vertical gray lines indicate the times at which the snapshots shown in Figure 14 are sampled.

To assess whether the depth-independent viscosity assumed in the mean state analysis is valid throughout the record, we infer vertical profiles of $R_+$ and $R_-$ at discrete times, following the same procedure as described in Section 5.1.2. The sampling times, chosen to capture the range of observed ellipse polarizations at CM1, are indicated by the vertical gray lines in Figure 13. We then compare the inferred and observed $R_-$ values at CM4, which provides an indication of the validity of the depth-independent viscosity assumption.

We begin by computing time series of $\delta_+$, and subsequently $\delta_-$, over the entire record (Figure 13c). As expected given the observed temporal variations in $R_+$ at CM1 and the way in which $\delta_+$ and $\delta_-$ are calculated, both time series exhibit temporal variability, and during some periods (e.g., between June and February 2016), they correlate clearly with variations in $R_+$ at CM1. However, there are also intervals when $\delta_+$ deviates from the expected trend and increases sharply beyond the water column thickness, resulting in $\delta_- \gg z_{CM1}$. Since only minimal differences in $R_-$ are observed between CM1 and CM4 (see solid and dashed green curves in Figure 13b), this points to a breakdown of the idealized constant viscosity solution described by Equation 16 during those periods. These events tend to coincide with above-average background flow (see red curve in Figure 13a) and close to circular tidal ellipses at CM1 (see black curve in Figure 13a). In fact, during periods of high flow, the ratio $R_+(z_{CM1})/R_+(z_{CM4})$ approaches zero (Figure 13b) and hence $\delta_+$ tends to infinity when estimated from Equation 17 due to a division by $\ln(1 - R_+(z_{CM1})/R_+(z_{CM4}))$. In summary, the time series of inferred viscous length scales suggest that the depth-independent viscosity assumption may be valid under low flow conditions, but fails when flow speeds are high.

This interpretation is supported by the inferred vertical profiles shown in Figures 14a–14c, sampled at times of low flow, average flow, and high flow, respectively. The shadings show the extent of the inferred $\delta_+$ (pink) and $\delta_-$ (green). During low and average flow conditions (Figures 14a and 14b), the CW and ACW rotary components are

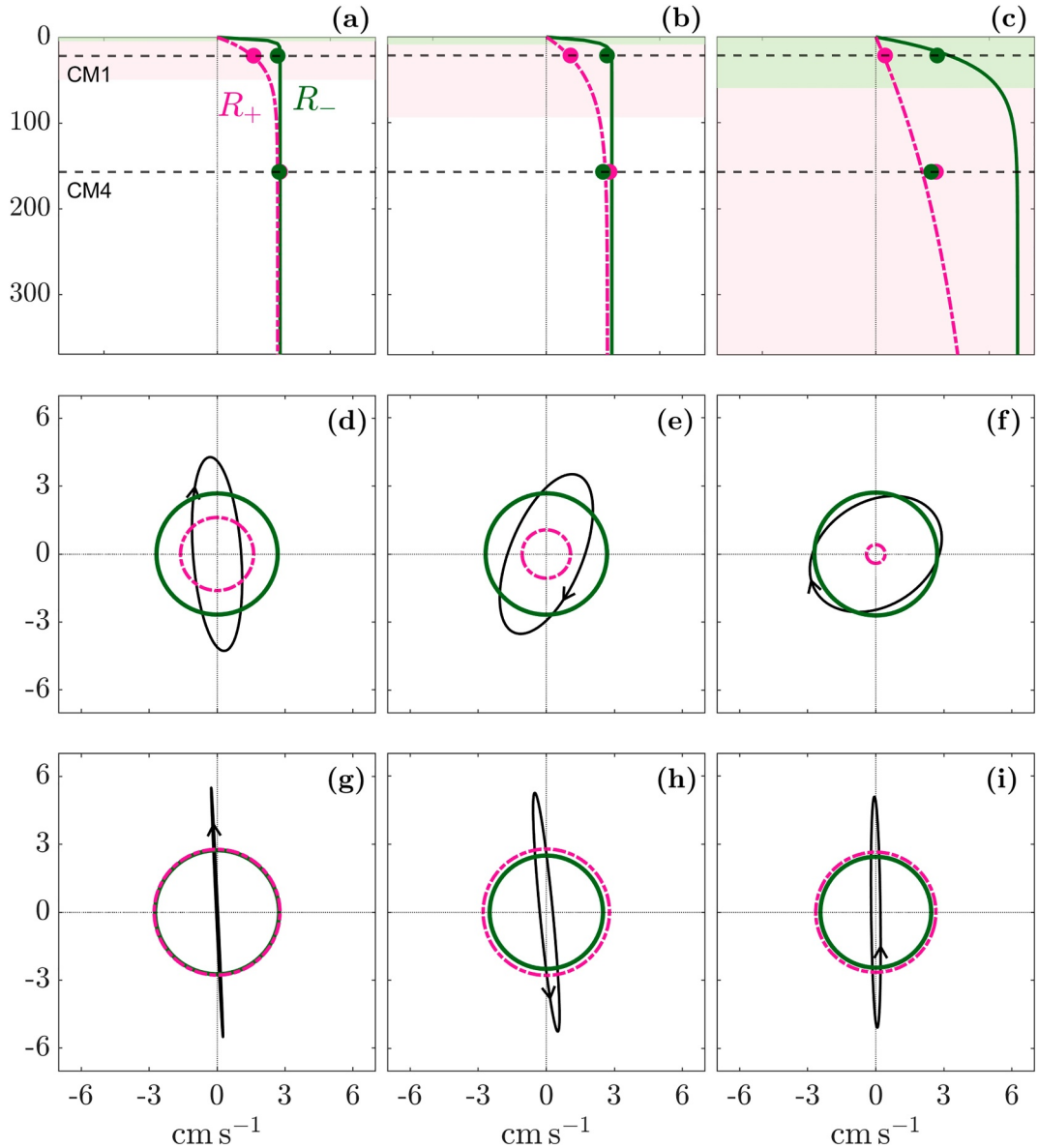


**Figure 14.** Schematic representation of vertical profiles of the anti-clockwise (ACW) rotary component amplitude $R_+$ (pink dashed) and clockwise (CW) rotary component amplitude $R_-$ (green solid) and observed tidal ellipses for the $M_2$ tidal constituents sampled at three different times within the observational record. The left-hand, middle, and right-hand column correspond to sampling times (1), (2), and (3) labeled in Figure 13. The markers in (a–c), as well as the ellipses and rotary components shown in (d–i) correspond to the values predicted by the moving-window harmonic analysis at CM1 and CM4 (see corresponding markers in Figure 13b). The shading indicates the estimated viscous length scales of the ACW component ($\delta_+$; pink shading) and of the CW component ($\delta_-$; green shading).

no longer influenced by boundary friction at CM4. The CW rotary component ($R_-$) reaches its free-stream value above CM1, whereas the ACW component ($R_+$) remains influenced by boundary friction at CM1. This is consistent with the observed CW tidal ellipses at CM1 (Figures 14d and 14e) and the nearly rectilinear ellipses at CM4 (Figures 14g and 14h), indicating that the inferred $R_{+/-}$ profiles, estimated based on an assumed depth-independent viscosity, are able to reproduce the observations at CM4 very well. Moreover, comparing the $R_+$ profiles in Figures 14a and 14b shows that the vertical extent over which boundary friction influences the rotary components increases with flow speed. Given that $\delta_- < z_{CM1}$ and $z_{CM1} < \delta_+ < z_{CM4}$ in both cases, the relative reduction in $R_+$ at CM1 compared with CM4 increases with flow, consistent with the slightly more circular ellipse at CM1 observed in the average flow snapshot (Figure 14e) compared with the low flow case (Figure 14d).

In contrast, during the high flow snapshot (right-hand column in Figure 14), the inferred $\delta_{+/-}$ values fail to produce profiles that satisfy both the boundary condition at the ice base ($R_+(0) = 0$) and the observed values at CM4 (Figure 14c). Consequently, the inferred profiles cannot simultaneously reproduce the observed nearly rectilinear ellipse at CM4 (Figure 14i) and the nearly circular ellipse at CM1 (Figure 14f). This discrepancy suggests that, during periods of high flow, the assumption of depth-independent viscosity breaks down, and viscosity likely varies with depth, as seen in one-dimensional model simulations beneath Filchner-Ronne Ice Shelf (Makinson, 2002).

Figure 13d shows the eddy viscosity, calculated from Equation 14 using the $\delta_+$ time series in Figure 13c. These inferred eddy viscosity values can be interpreted as representing the effective eddy viscosity associated with an under-ice Ekman boundary layer, that is, they capture the influence of boundary friction on the total flow (including both tidal and nontidal flow components). As such, the inferred viscosity can be used to estimate the Ekman depth from $\sqrt{2\nu/|f|}$, as shown by the cyan line in Figure 13c. Excluding the periods of high flow during which the depth-independent viscosity model breaks down and the inferred viscosity becomes unrealistically large, the estimated eddy viscosity is approximately 0.01 $m^2\ s^{-1}$, yielding an Ekman depth of ∼12 m.

Although few observationally derived estimates of eddy viscosity exist for comparison, Davis et al. (2023) recently reported an estimate of $0.0009 \pm 0.0005\ m^2\ s^{-1}$ from beneath Thwaites Glacier, obtained by fitting an analytical Ekman layer model to velocity profiles measured through the ice shelf-ocean boundary layer. This value is one order of magnitude smaller than the value estimated here. However, the Thwaites cavity environment, characterized by strong thermal driving (>1.5°C), weak current forcing (∼2 cm $s^{-1}$), and strong near-ice stratification, significantly differs from conditions at Site 5c, making direct comparison uncertain. Under Ronne Ice Shelf, no observational eddy viscosity estimates are available. However, Makinson (2002) reported modeled values beneath Ronne Ice Shelf up to $\sim 0.07\ m^2\ s^{-1}$ based on a turbulence closure model that accounts for critical latitude effects on tidal vertical mixing. Our inferred values during low flow periods fall within this modeled range, supporting that our estimates are plausible, though further observations would be needed to confirm this.

During periods of low to near-average flow (when the depth-independent viscosity assumption appears valid), the Ekman depth remains relatively steady and shallower than CM1. We will return to this point in Section 6, where we consider how the enhanced influence of boundary friction on semidiurnal tides affects the choice of depth at which to sample ocean conditions applied in the three-equation melt rate formulation.

### 5.2. Depth-Dependence of the Tidal Current Magnitude

The analysis presented in the previous section suggests that, for a given tidal constituent, the observed changes in tidal ellipse properties between CM1 and CM4 largely depend on the distance of CM1 from the ice base relative to the distance over which viscosity influences the ACW rotary component. This distance, which we termed viscous length scale $\delta_+$, in turn appears to be influenced by the background current strength. We now evaluate how this constituent-specific frictional effect, may be reflected in the vertical structure of the total tidal current magnitude, which represents the combined influence of all tidal constituents rather than each in isolation. Note that for the purpose of the discussion presented here, we interpret conditions at CM4 as being representative of the free-stream tidal current magnitude (justified by the nearly rectilinear dominant $M_2$ tidal ellipse at CM4 throughout the record).

Figure 15 presents the tidal current magnitude at CM1 and CM4 (top row), and the two orthogonal tidal current components at CM1 (middle row) and at CM4 (bottom row), with each column showing one fortnightly spring-neap cycle sampled at a different time within the observational record. The vertical gray lines, labeled (1), (2), and (3), in Figure 15 coincide with the vertical gray lines in Figure 13 and with the timings of the snapshots shown in Figure 14. As such, the left-hand column in Figure 15 corresponds to low flow conditions, the middle column reflects near average flow conditions, and the right-hand column shows high flow conditions. Moreover, based on the analysis presented in Figure 14, the left-hand and middle columns show periods during which the depth-independent viscosity assumption appears to hold, whereas the right-hand column shows a case in which this assumption fails.

Starting with a description of the free-stream conditions, as expected based on the mixed diurnal and semidiurnal tides, the north-south component ($v_{tide}$) features two northward and southward flows per day, with relatively pronounced differences between consecutive tidal peaks and troughs (yellow curves in Figures 15g–15i). In line

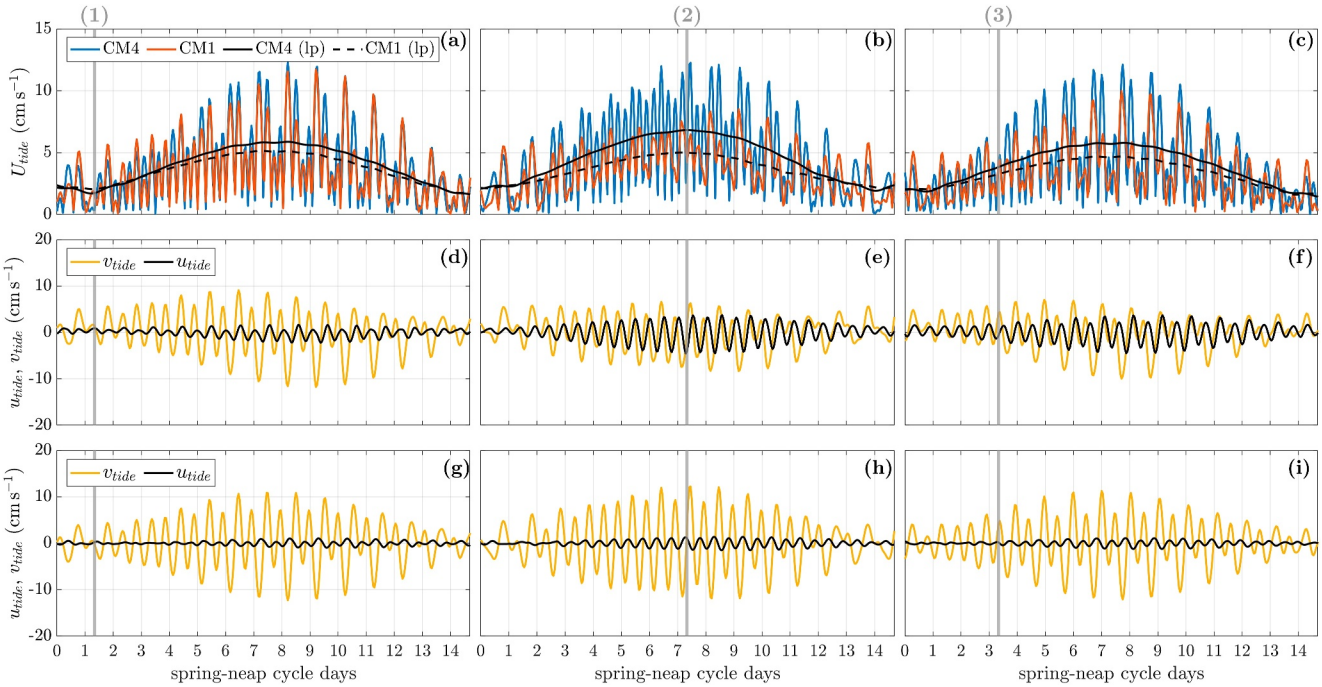


**Figure 15.** Tidal current speed $U_{tide} = \sqrt{u_{tide}^2 + v_{tide}^2}$ at CM1 and CM4 with orange and blue curves showing unfiltered data and black dashed and solid curves showing 36-hr low-pass filtered data (a–c), and tidal current components $u_{tide}$ and $v_{tide}$ at CM1 (d–f) and CM4 (g–i), sampled over one 14.76-day spring-neap cycle at three different times within the observational record. The vertical gray lines labeled (1), (2), and (3) correspond to the sample times indicated by the vertical gray lines in Figure 13.

with the nearly rectilinear diurnal and semidiurnal tidal ellipses at CM4, the east-west component of the tide ($u_{tide}$) is negligible at this depth (black curves in Figures 15g–15i). Given that speed peaks twice during an oscillating current, the tidal current speed $U_{tide}$ (blue curves in Figures 15a–15c) features a 4 cpd signal. Furthermore, the three cases display a clear spring-neap cycle at CM4 with the largest peak-to-through variations in $U_{tide}$ occurring during spring tides (around day 7 of the cycle). The minimal differences between the tidal signal at CM4 in the three instances shown in Figure 15 supports the previous assumption that CM4 is positioned beyond the region of boundary friction influence.

Comparing the orange and blue curves in Figures 15a–15c shows that friction at the ice base causes a reduction in the peak-to-trough variations of $U_{tide}$. This is consistent with the smaller differences between $u_{tide}$ and $v_{tide}$ at CM1 compared with CM4 (particularly apparent in Figures 15e and 15f), as well as with the transition of the semi-diurnal tidal ellipse from near-rectilinear at CM4 to more circular at CM1. This suppression of tidal current sub-daily variability near the ice base suggests that melt rate variability at tidal frequencies (which cannot be observed directly in the ApRES-derived time series) is likely not as pronounced as the sub-daily variability in free-stream tidal current magnitude.

In addition to this friction-induced reduction in tidal current sub-daily variability, the 36-hr low-pass filtered tidal current magnitudes at CM1 and CM4 (black dashed and solid lines in Figures 15a–15c) show that the tidal current strength is also reduced relative to free-stream conditions, although the reduction is relatively small. This attenuation appears to be driven primarily by a reduction in $v_{tide}$, whereas $u_{tide}$ at CM1 is slightly enhanced relative to CM4. This relative enhancement in $u_{tide}$ is consistent with the larger peaks of energy at CM1 compared with CM4 visible in the $u$-component PSD plots (Figure 8).

The spring-neap modulation in both sub-daily variability and strength of the tidal current is most pronounced during spring tides. Moreover, although $U_{tide}$ is generally lower at CM1 than at CM4, as expected from friction-induced attenuation, Figures 15a–15c reveals instances around neap tides when CM1 values exceeds those at CM4. This apparent amplification of the near-ice tidal current magnitude relative to the free-stream may reflect friction-induced shifts in the frequency and/or phase of the tidal current between CM1 and CM4. Further evidence

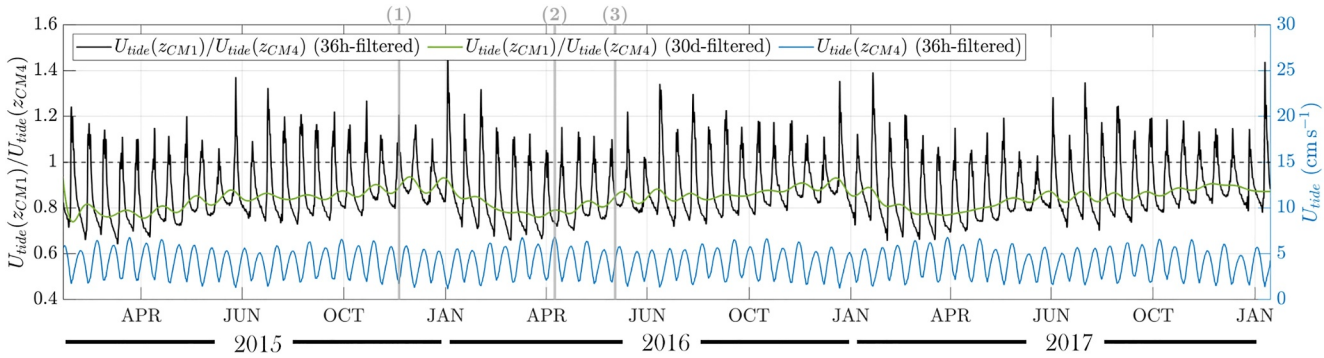


**Figure 16.** Ratio between the tidal current speed at CM1 and CM4 over the 3-year record, calculated based on 36-hr low-pass filtered (black curve) and 30-day low-pass filtered (green curve) time series. The 36-hr low-pass filtered tidal current magnitude at CM4 (blue curve) is also included. The vertical gray lines labeled (1), (2), and (3) correspond to the times indicated by the vertical gray lines in Figures 13 and 15.

of this spring-neap modulation is provided in Figure 16, which shows the ratio of 36-hr low-pass filtered $U_{tide}$ between CM1 and CM4 (black curve), as well as the tidal current magnitude at CM4 (blue curve). The pattern of stronger attenuation during spring tides and relative enhancement during neap tides, evident in the three spring-neap cycles shown in Figure 15, emerges consistently throughout the 3-year record.

Comparing the cases where eddy viscosity can be assumed to be constant (Figures 15a and 15b) suggests that the friction-induced attenuation increases with background flow strength. This is consistent with the larger reduction in $R_+$ at CM1 relative to the free-stream under near-average versus low flow conditions (Figures 14a and 14b). However, comparing Figures 15b and 15c shows that when the viscosity profiles differ, stronger background flow does not necessarily lead to enhanced attenuation, suggesting that the viscosity profile influences the frictional effect. These qualitative observations are supported by the ratio of mean $U_{tide}$ at CM1 to that at CM4 over the spring-neap cycle, which is 93%, 79%, and 85% in Figure 15a–15c, respectively. This variability in the degree of attenuation is evident throughout the record, particularly during spring tides when attenuation is strongest (see changes in the minima of the black curve in Figure 16). Nevertheless, both the variability and the overall level of attenuation are relatively small, as indicated by the 30-day low-pass filtered $U_{tide}$ ratio averaging 84% and remaining within a range of 74%–94% over the 3-year record (green curve in Figure 16).

In summary, ice base friction acts to dampen both high frequency tidal fluctuations and the mean tidal current magnitude. Although the attenuation of the time-averaged tidal current magnitude varies over the spring-neap cycle and on longer timescales, it remains relatively weak. This reflects friction-induced changes in the near-ice semidiurnal tidal ellipses, which primarily involve changes in polarization rather than changes in ellipse size.

## 6. Summary and Discussion

This study utilizes a multi-year data set of oceanographic and glaciological observations from Site 5c beneath Ronne Ice Shelf to characterize the local water column structure and dynamics, to examine basal melt rate variability across a range of timescales, and to investigate the influence of ice base friction on the vertical structure of tidal currents. The data set includes three years of temperature, salinity, and current measurements from a sub-ice shelf mooring, along with one year of basal melt rate estimates derived from ApRES radar measurements. By applying a calibrated velocity-dependent melt rate parameterization (Jenkins et al., 2010), the ApRES-derived melt rates time series is extended, resulting in a 3-year contemporaneous record of ocean conditions and basal melt rates.

Building on prior surveys of the study site, we provide a detailed description of the water column, identifying two distinct water masses: Berkner-sourced ISW near the ice base and Ronne-sourced ISW near the seafloor. A notable feature of the water column at Site 5c is a warm layer near the ice base, evident in the CTD profile. The temperature time series from the upper two CT mooring sensors suggest that the strength of this warm feature varies over time, likely with a seasonal cycle. Future mooring designs at this site could prioritize placing CMs and CT sensors through this layer to further examine the processes controlling its variability. Unlike sites near Ronne Ice Front, which exhibit stronger stratification with pronounced seasonal variability (Makinson et al., 2006), Site

5c features a weakly stratified water column with minimal changes in density structure throughout the 3-year observational period. Harmonic analysis of the current measurements indicates mixed semidiurnal tides with strong spring-neap variability, superimposed onto a dominant nontidal background flow. The ApRES-derived basal melt rate measurements also exhibit strong spring-neap variability, consistent with the spring-neap modulation of the near-ice current speed and the strong correlation between melt rates and current speed at this site.

Using the velocity measurements from the two CMs installed on the mooring, we assess ice base friction-induced changes in the rotational properties and magnitude of the tidal current. Unlike the diurnal tidal ellipses, which feature minimal changes between the two sensors, the semidiurnal ellipses exhibit marked changes with depth, transitioning from nearly rectilinear in the free-stream portion of the water column to more circular and CW-rotating near the ice base. These observed depth variations are linked to the enhanced differential effects of boundary friction on the CW and ACW rotary components of the semidiurnal tides due to proximity of the study site to the semidiurnal critical latitudes. A theoretical model, which accounts for these effects, and assumes depth-independent eddy viscosity, is able to reproduce the observed depth variations of the 3-year mean tidal ellipse characteristics.

In addition to the depth-dependence of the mean state, we observe temporal variability in the semidiurnal tidal ellipse properties at the upper CM (CM1). In particular, the polarization of the dominant semidiurnal tide varies over seasonal timescales, suggesting changes in the vertical extent over which viscosity affects the ACW component. We hypothesize that this variability is linked to low-frequency changes in the nontidal background flow, which would be expected to modulate the eddy viscosity.

Although the analysis of tidal ellipse variability is limited to timescales longer than ∼30 days, variations in the total tidal current magnitude reveal that frictional effects also vary on shorter timescales. Specifically, ice base friction attenuates both the time-averaged tidal current and the magnitude of tidal fluctuations, with stronger attenuation observed during spring tides. However, the overall reduction in tidal current strength remains relatively small, with the 30-day low-pass filtered near-ice tidal current magnitude averaging 84% of the free-stream value over the 3-year record. This relatively weak attenuation in the mean tidal flow is consistent with the friction-induced changes in the near-ice semidiurnal tidal ellipses, which primarily involve changes in polarization rather than substantial changes in ellipse size.

We show that the theoretical framework used to interpret tidal ellipse properties also enables, in principle, the estimation of eddy viscosity from current measurements at only two depths. During periods of low to moderate background flow, the model yields plausible viscosity estimates. However, under strong background flow, it yields unrealistically large values, indicating a breakdown of the depth-independent viscosity assumption in more energetic conditions. Further work is needed to validate the proposed approach for inferring eddy viscosity from current measurements at only two depths, particularly by clarifying the conditions under which the depth-independent viscosity assumption holds or fails. Validation could be achieved through direct comparison with viscosity estimates derived from near-ice current profiles (e.g., as in Davis et al. (2023)) or via controlled numerical experiments spanning a range of flow regimes. If validated, this method could offer a practical means of estimating eddy viscosity from moored CM records collected near critical latitudes.

Our analysis of the vertical structure of the tidal ellipses shows that the influence of boundary friction on the semidiurnal tidal constituents extends beyond the uppermost CM, as indicated by $\delta_+$ values that exceed the depth of CM1 throughout the 3-year record. This raises questions about how the enhanced frictional influence on the anticlockwise component of the semidiurnal tide affects the overall boundary layer thickness quantified by the Ekman depth, and the implications this may have for the choice of instrument at which to sample the velocity driving the three-equation melt rate formulation. The friction velocity parameterization in Equation 1 requires the flow speed outside the logarithmic layer, which occupies the top ∼10% of the boundary layer (McPhee, 2008). If the large $\delta_+$ values lead to a thicker overall boundary layer such that CM1 lies within the logarithmic layer, then using velocity measurements from CM1 would not satisfy the underlying assumptions of the parameterization, and deeper measurements from CM4 might be more appropriate. However, estimating the Ekman depth from $\sqrt{2\nu/|f|}$ using an eddy viscosity value inferred from the theoretical framework described above suggests an Ekman depth of approximately 12 m. This places CM1 below the base of the Ekman layer, indicating that measurements at the upper CM are likely taken outside the logarithmic layer, and are therefore suitable for use in the three-equation melt rate formulation. Moreover, it is worth noting that using velocities from CM4 would likely

lead to inaccuracies in the melt rate time series, as the friction velocity parameterization in Equation 1 does not account for the depth-dependent changes in tidal ellipse polarization observed between CM4 and CM1.

More broadly, this discussion highlights knowledge gaps in how constituent-specific viscous length scales ($\delta_+$ and $\delta_-$) relate to the total boundary layer thickness. In particular, it remains unknown whether enhanced ice base friction associated with proximity to critical latitudes may lead to thicker Ekman layers in certain environments, especially where tides dominate the flow. Soulsby (1983) proposed an effective boundary layer thickness based on a weighted average of the frictional effects on the anticlockwise and CW components, $\delta = (R_+\delta_+ + R_-\delta_-)/(R_+ + R_-)$. However, this formulation applies only to individual tidal constituents, and how these $\delta$ values combine to define the overall boundary layer structure remains unclear. Addressing these uncertainties through a combination of targeted observations and numerical simulations across a range of tidal regimes would help ensure that critical latitude effects are accounted for when choosing the depth of the oceanographic measurements applied to the three-equation melt formulation.

Having examined the implications of our results on the application of the three-equation melt rate formulation to observational data, we now consider the implications for the parameterization of tides in numerical models. Tidal currents are often omitted from regional and circum-Antarctic ocean model simulations to reduce computational cost. In such cases, a common approach to account for their effect on basal melt rates is to modify the parameterization of ocean heat and salt fluxes in the three-equation melt rate formulation by adding a tidal factor into the friction velocity expression, as originally proposed by Jenkins et al. (2010):

$$u_* = \sqrt{C_d(U_{nt}^2 + U_{bt}^2)}, \tag{18}$$

where $U_{nt}$ is the simulated current (which excludes tides) and $U_{bt}$ corresponds to a time-averaged, spatially varying estimate of the barotropic tidal current speed. Parameterizing tidal effects on basal melt rates via Equation 18 assumes that tidal currents enhance basal melting primarily by increasing shear at the ice shelf base, rather than by modifying thermal driving. At Site 5c, this assumption is largely supported by the decomposition analysis presented in Figure 10, which identifies variations in near-ice flow speed as the dominant driver of tide-induced basal melt rate variability. Nonetheless, tide-induced variations in thermal driving, particularly over the spring-neap cycle, also contribute non-negligibly to the melt rate variability. Equation 18 is typically implemented with a drag coefficient $C_d$ that is constant in both space and time. A spatially uniform drag coefficient does not account for enhanced frictional effects near critical latitudes, as observed at Site 5c, potentially leading to underestimated area-averaged tide-induced basal melt rates. Similarly, assuming a temporally constant drag coefficient neglects the time-varying influence of friction on tidal currents driven by temporal changes in near-ice tidal ellipse polarization, as observed at Site 5c. That said, for studies focused on estimating time-averaged melt rates, the use of a temporally constant drag coefficient in combination with a time-averaged barotropic tidal current speed is probably justified, despite limiting the representation of near-ice tidal current variability and its influence on basal melt rates.

The preceding discussion has highlighted that the three-equation melt rate formulation, implemented with a modified friction velocity formulation to parameterize tidal effects, lacks the physics required to fully capture the latitude-dependent influence of boundary friction on the vertical structure of the tidal current ellipse. Since tidal vertical mixing, and therefore tide-induced basal melt rates, depend not only on the mean tidal current magnitude but also on tidal ellipse polarization (Makinson, 2002), developing a new parameterization that accounts for this effect would improve the representation of both spatial and temporal variability in tide-driven basal melt rates. Specifically, such a parameterization would relate the barotropic tidal ellipse to the tidal ellipse just beyond the logarithmic layer, providing a more accurate velocity input to the three-equation melt rate formulation. The constant viscosity model applied in Section 5 provides a useful starting point for the derivation of such a parameterization, as it was shown to capture the time-averaged influence of ice base friction on the vertical structure of the tidal ellipses at Site 5c. However, because it treats each tidal constituent independently, the model would need to be extended to account for the combined effects of multiple constituents on the total tidal current. In addition, further work is needed to clarify conditions under which the depth-independent viscosity assumption holds, as previously discussed.

To conclude, the study presented in this paper, based on a single sub-ice shelf mooring site located near the critical latitudes of the semidiurnal tides, enhances our understanding of how tides modulate basal melt rate variability, and highlights how boundary friction beneath an ice shelf base impacts the barotropic tidal ellipse. Our results highlight limitations of a friction velocity-based tidal melt rate parameterization, which estimates the friction-induced departure from the barotropic tidal current via a constant drag coefficient. Extending the analyses presented here with observations from additional sites spanning a range of tidal regimes would provide a stronger basis for generalizing our findings and improving the representation of tidal vertical mixing, and hence tide-induced basal melting, in models that do not explicitly resolve tides.

## Appendix A: Parameterized Melt Rate

Section 2.3 describes the approach taken to estimate basal melt rates from 36-hr low-pass filtered observed ocean conditions at CM1 and CT1. Figure A1 shows the distribution of the resulting melt rate estimates as a function of the ApRES-derived melt rates for the year 2015.

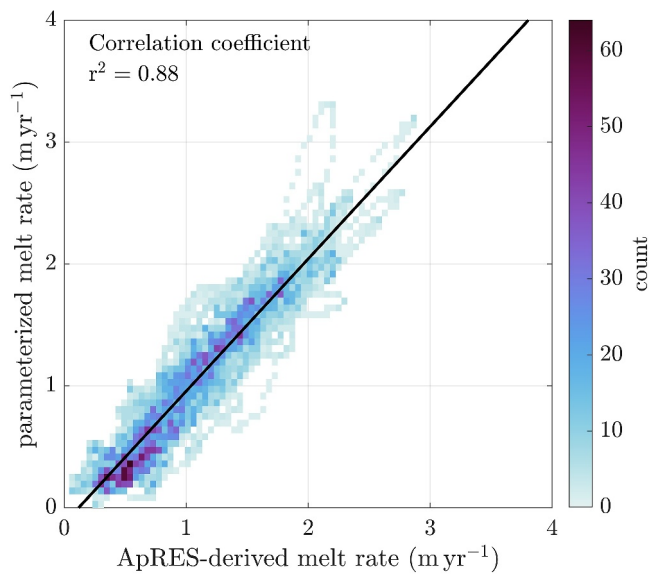


**Figure A1.** Parameterized and observed basal melt rate distributions over the year 2015.

## Data Availability Statement

The ApRES basal melt rate time series presented in this study is available at https://doi.org/10.6084/m9.figshare.28350665. The processed mooring data presented in the paper are available at https://doi.org/10.6084/m9.figshare.28350683. The map in Figure 1 was created using the Antarctic Mapping Tools toolbox (Greene et al., 2017) available on GitHub at https://github.com/chadagreene/Antarctic-Mapping-Tools with water column thickness data obtained from the MEaSUREs BedMachine Antarctic Version 3 data set (Morlighem et al., 2017) available at doi:10.1002/2017gl074954.

**Acknowledgments**
JA is supported by a C-CLEAR Doctoral Partnership studentship from the Natural Environmental Research Council. SØ is supported by the Horizon Europe Funding Program for research and innovation under grant agreement N° 101060452 OCEAN:ICE.

## References

Akhoudas, C., Sallée, J. B., Reverdin, G., Aloisi, G., Benetti, M., Vignes, L., & Gelado, M. (2020). Ice shelf basal melt and influence on dense water outflow in the southern Weddell Sea. *Journal of Geophysical Research: Oceans*, *125*(2), e2019JC015710. https://doi.org/10.1029/2019JC015710

Arzeno, I., Beardsley, R. C., Limeburner, R., Owens, B., Padman, L., Spring, S. R., et al. (2014). Ocean variability contributing to basal melt rate near the ice front of ross ice shelf, Antarctica. *Journal of Geophysical Research: Oceans*, *119*(7), 4214–4233. https://doi.org/10.1002/2014jc009792

Brennan, P. V., Lok, L. B., Nicholls, K., & Corr, H. (2014). Phase-sensitive FMCW radar system for high-precision antarctic ice shelf profile monitoring. *IET Radar, Sonar & Navigation*, *8*(7), 776–786. https://doi.org/10.1049/iet-rsn.2013.0053

Corr, H. F., Jenkins, A., Nicholls, K. W., & Doake, C. S. (2002). Precise measurement of changes in ice-shelf thickness by phase-sensitive radar to determine basal melt rates. *Geophysical Research Letters*, *29*(8), 73-1–4. https://doi.org/10.1029/2001GL014618

Davis, P. E., Jenkins, A., Nicholls, K. W., Brennan, P. V., Abrahamsen, E. P., Heywood, K. J., et al. (2018). Variability in basal melting beneath Pine Island Ice Shelf on weekly to monthly timescales. *Journal of Geophysical Research: Oceans*, *123*(11), 8655–8669. https://doi.org/10.1029/2018JC014464

Davis, P. E., & Nicholls, K. W. (2019). Turbulence observations beneath Larsen C Ice Shelf, Antarctica. *Journal of Geophysical Research: Oceans*, *124*(8), 5529–5550. https://doi.org/10.1029/2019JC015164

Davis, P. E., Nicholls, K. W., Holland, D. M., Schmidt, B. E., Washam, P., Riverman, K. L., et al. (2023). Suppressed basal melting in the eastern Thwaites Glacier grounding zone. *Nature*, *614*(7948), 479–485. https://doi.org/10.1038/s41586-022-05586-0

Depoorter, M. A., Bamber, J. L., Griggs, J. A., Lenaerts, J. T., Ligtenberg, S. R., Van Den Broeke, M. R., & Moholdt, G. (2013). Calving fluxes and basal melt rates of Antarctic ice shelves. *Nature*, *502*(7469), 89–92. https://doi.org/10.1038/nature12567

Foldvik, A., Gammelsrød, T., Nygaard, E., & Østerhus, S. (2001). Current measurements near Ronne Ice Shelf: Implications for circulation and melting. *Journal of Geophysical Research*, *106*(C3), 4463–4477. https://doi.org/10.1029/2000jc000217

Foldvik, A., Gammelsrød, T., & Tørresen, T. (1985). Circulation and water masses on the Southern Weddell Sea Shelf. In J. S. Stanley (Ed.), *Oceanology and water masses on the southern weddell sea shelf* (pp. 5–20). American Geophysical Union.

Foreman, M. G. G. (1978). Manual for tidal currents analysis and prediction. In *Pacific marine science report 78-6 (2004revision*. Institute of Ocean Sciences. Retrieved from https://www.researchgate.net/publication/264782849

Gade, H. G. (1979). Melting of ice in sea water: A primitive model with application to antarctic ice shelf and icebergs. *American Meteorological Society*.

Gammelsrød, T., Foldvik, A., Nøst, O. A., Foldvik, Ø., Anderson, L. G., Fogelqvist, E., et al. (1994). Distribution of water masses on the continental shelf in the southern Weddell Sea. In *The Polar Oceans and Their Role in Shaping the Global Environment* (Vol. 85, pp. 159–176). https://doi.org/10.1029/GM085p0159

Godin, G. (1972). *The analysis of tides*. University of Toronto Press.

Gonella, J. (1972). A rotary-component method for analysing meteorological and oceanographic vector time series. *Deep-Sea Research and Oceanographic Abstracts*, *19*(12), 833–846. https://doi.org/10.1016/0011-7471(72)90002-2

Greene, C. A., Gwyther, D. E., & Blankenship, D. D. (2017). Antarctic mapping tools for Matlab. *Computers and Geosciences*, *104*, 151–157. https://doi.org/10.1016/j.cageo.2016.08.003

Gwyther, D. E., Cougnon, E. A., Galton-Fenzi, B. K., Roberts, J. L., Hunter, J. R., & Dinniman, M. S. (2016). Modelling the response of ice shelf basal melting to different ocean cavity environmental regimes. *Annals of Glaciology*, *57*(73), 131–141. https://doi.org/10.1017/aog.2016.31

Hattermann, T., Nicholls, K. W., Hellmer, H. H., Davis, P. E., Janout, M. A., Østerhus, S., et al. (2021). Observed interannual changes beneath Filchner-Ronne Ice Shelf linked to large-scale atmospheric circulation. *Nature Communications*, *12*(1), 2961. https://doi.org/10.1038/s41467-021-23131-x

Hausmann, U., Sallée, J. B., Jourdain, N. C., Mathiot, P., Rousset, C., Madec, G., et al. (2020). The role of tides in ocean-ice shelf interactions in the Southwestern Weddell Sea. *Journal of Geophysical Research: Oceans*, *125*(6), 1–29. https://doi.org/10.1029/2019JC015847

Huot, P. V., Fichefet, T., Jourdain, N. C., Mathiot, P., Rousset, C., Kittel, C., & Fettweis, X. (2021). Influence of ocean tides and ice shelves on ocean–ice interactions and dense shelf water formation in the D'Urville Sea, Antarctica. *Ocean Modelling*, *162*, 101794. https://doi.org/10.1016/j.ocemod.2021.101794

Janout, M. A., Hellmer, H. H., Hattermann, T., Huhn, O., Sültenfuss, J., Østerhus, S., et al. (2021). FRIS revisited in 2018: On the circulation and water masses at the Filchner and Ronne Ice Shelves in the southern Weddell Sea. *Journal of Geophysical Research: Oceans*, *126*(6), e2021JC017269. https://doi.org/10.1029/2021JC017269

Jenkins, A., Nicholls, K. W., & Corr, H. F. (2010). Observation and parameterization of ablation at the base of Ronne Ice Ahelf, Antarctica. *Journal of Physical Oceanography*, *40*(10), 2298–2312. https://doi.org/10.1175/2010JPO4317.1

Jourdain, N. C., Molines, J. M., Le Sommer, J., Mathiot, P., Chanut, J., de Lavergne, C., & Madec, G. (2019). Simulating or prescribing the influence of tides on the Amundsen Sea ice shelves. *Ocean Modelling*, *133*(October 2018), 44–55. https://doi.org/10.1016/j.ocemod.2018.11.001

Kim, T., Hong, J. S., Jin, E. K., Moon, J. H., Song, S. K., & Lee, W. S. (2023). Spatiotemporal variability in ocean-driven basal melting of cold-water cavity ice shelf in Terra Nova Bay, East Antarctica: Roles of tide and cavity geometry. *Frontiers in Marine Science*, *10*. https://doi.org/10.3389/fmars.2023.1249562

Kopte, R., Becker, M., Holtermann, P., & Winter, C. (2022). Tides, stratification, and counter rotation: The German Bight ROFI in comparison to other Regions of Freshwater Influence. *Journal of Geophysical Research: Oceans*, *127*(6), e2021JC018236. https://doi.org/10.1029/2021JC018236

Maas, L. R., & van Haren, J. J. (1987). Observations on the vertical structure of tidal and inertial currents in the central North Sea. *Journal of Marine Research*, *45*(2), 293–318. https://doi.org/10.1357/002224087788401106

Makinson, K. (2002). Modeling tidal current profiles and vertical mixing beneath Filchner-Ronne Ice Shelf, Antarctica. *Journal of Physical Oceanography*, *32*(1), 202–215. https://doi.org/10.1175/1520-0485(2002)032⟨0202:MTCPAV⟩2.0.CO;2

Makinson, K., Holland, P. R., Jenkins, A., Nicholls, K. W., & Holland, D. M. (2011). Influence of tides on melting and freezing beneath Filchner-Ronne Ice Shelf, Antarctica. *Geophysical Research Letters*, *38*(6), 4–9. https://doi.org/10.1029/2010GL046462

Makinson, K., & Nicholls, K. W. (1999). Modeling tidal currents beneath Filchner-Ronne Ice Shelf and on the adjacent continental shelf: Their effect on mixing and transport. *Journal of Geophysical Research*, *104*(C6), 13449–13465. https://doi.org/10.1029/1999jc900008

Makinson, K., Schröder, M., & Øterhus, S. (2006). Effect of critical latitude and seasonal stratification on tidal current profiles along Ronne Ice Front, Antarctica. *Journal of Geophysical Research*, *111*(3), 1–15. https://doi.org/10.1029/2005JC003062

Malyarenko, A., Wells, A. J., Langhorne, P. J., Robinson, N. J., Williams, M. J., & Nicholls, K. W. (2020). A synthesis of thermodynamic ablation at ice–ocean interfaces from theory, observations and models. *Ocean Modelling*, *154*(July), 101692. https://doi.org/10.1016/j.ocemod.2020.101692

McDougall, T. J., & Barker, P. M. (2011). *Getting started with TEOS-10 and the Gibbs seawater (GSW) oceanographic toolbox*. Trevor J McDougall.

McDougall, T. J., Barker, P. M., Feistel, R., & Galton-Fenzi, B. K. (2014). Melting of ice and sea ice into seawater and frazil ice formation. *Journal of Physical Oceanography*, *44*(7), 1751–1775. https://doi.org/10.1175/JPO-D-13-0253.1

McPhee, M. (2008). *Air-Ice-Ocean interaction: Turbulent Ocean boundary layer exchange processes*. Springer.

McPhee, M., Maykut, G. A., & Morison, J. H. (1987). Dynamics and thermodynamics of the ice/upper ocean system in the marginal ice zone of the Greenland Sea. *Journal of Geophysical Research*, *92*(C7), 7017–7031. https://doi.org/10.1029/JC092iC07p07017

Morlighem, M., Williams, C. N., Rignot, E., An, L., Arndt, J. E., Bamber, J. L., et al. (2017). BedMachine v3: Complete bed topography and Ocean bathymetry mapping of Greenland from Multibeam Echo sounding combined with mass conservation. *Geophysical Research Letters*, *44*(21), 11051–11061. https://doi.org/10.1002/2017GL074954

Mueller, R. D., Hattermann, T., Howard, S. L., & Padman, L. (2018). Tidal influences on a future evolution of the Filchner-Ronne Ice Shelf cavity in the Weddell Sea, Antarctica. *The Cryosphere*, *12*(2), 453–476. https://doi.org/10.5194/tc-12-453-2018

Mueller, R. D., Padman, L., Dinniman, M. S., Erofeeva, S. Y., Fricker, H. A., & King, M. A. (2012). Impact of tide-topography interactions on basal melting of Larsen C Ice Shelf, Antarctica. *Journal of Geophysical Research*, *117*(5), 1–20. https://doi.org/10.1029/2011JC007263

Munk, W. H., & Cartwright, D. (1966). Tidal spectroscopy and prediction. *Philosophical Transactions of the Royal Society of London*, *259*(1105), 533–581. Retrieved from https://royalsocietypublishing.org/

Munk, W. H., Zetler, B., & Groves, G. W. (1965). Tidal cusps. *Geophysical Journal of the Royal Astronomical Society*, *10*(2), 211–219. https://doi.org/10.1111/j.1365-246X.1965.tb03062.x

Nicholls, K. W., Corr, H. F., Stewart, C. L., Lok, L. B., Brennan, P. V., & Vaughan, D. G. (2015). Instruments and methods: A ground-based radar for measuring vertical strain rates and time-varying basal melt rates in ice sheets and shelves. *Journal of Glaciology*, *61*(230), 1079–1087. https://doi.org/10.3189/2015JoG15J073

Nicholls, K. W., Makinson, K., & Johnson, M. R. (1997). New oceanographic data from beneath Ronne Ice Shelf, Antarctica. *Geophysical Research Letters*, *24*(2), 167–170. https://doi.org/10.1029/96GL03922

Nicholls, K. W., Østerhus, S., Makinson, K., & Johnson, M. R. (2001). Oceanographic conditions south of Berkner Island, beneath Filchner-Ronne Ice Shelf, Antarctica. *Journal of Geophysical Research*, *106*(C6), 11481–11492. https://doi.org/10.1029/2000jc000350

Nixdorf, U., Oerter, H., & Miller, H. (1994). First access to the ocean beneath Ekstromisen, Antarctica, by means of hot-water drilling. *Annals of Glaciology*, *20*, 110–114. https://doi.org/10.3189/1994aog20-1-110-114

Nøst, O. A., & Foldvik, A. (1994). A model of ice shelf-ocean interaction with application to the Filcher-Ronne and Ross ice shelves. *Journal of Geophysical Research*, *99*(C7), 14243–14254. https://doi.org/10.1029/94jc00769

Padman, L., Siegfried, M. R., & Fricker, H. A. (2018). Ocean tide influences on the Antarctic and Greenland Ice Sheets. *Reviews of Geophysics*, *56*(1), 142–184. https://doi.org/10.1002/2016RG000546

Pawlowicz, R., Beardsley, B., & Lentz, S. (2002). Classical tidal harmonic analysis including error estimates in MATLAB using T TIDE. [Tech. Rep.]. *Computers and Geosciences*, *28*(8), 929–937. https://doi.org/10.1016/S0098-3004(02)00013-4

Prandle, D. (1982). The vertical structure of tidal currents and other oscillatory flows. *Continental Shelf Research*, *1*(2), 191–207. https://doi.org/10.1016/0278-4343(82)90004-8

Pritchard, H. D., Ligtenberg, S. R., Fricker, H. A., Vaughan, D. G., Van Den Broeke, M. R., & Padman, L. (2012). Antarctic ice-sheet loss driven by basal melting of ice shelves. *Nature*, *484*(7395), 502–505. https://doi.org/10.1038/nature10968

Reese, R., Gudmundsson, G. H., Levermann, A., & Winkelmann, R. (2018). The far reach of ice-shelf thinning in Antarctica. *Nature Climate Change*, *8*(1), 53–57. https://doi.org/10.1038/s41558-017-0020-x

Renfrew, I. A., King, J. C., & Markus, T. (2002). Coastal polynyas in the southern Weddell Sea: Variability of the surface energy budget. *Journal of Geophysical Research*, *107*(C6), 16-1–22. https://doi.org/10.1029/2000jc000720

Richter, O., Gwyther, D. E., King, M. A., & Galton-Fenzi, B. K. (2022). The impact of tides on Antarctic ice shelf melting. *The Cryosphere*, *16*(4), 1409–1429. https://doi.org/10.5194/tc-16-1409-2022

Robertson, R. (2013). Tidally induced increases in melting of Amundsen Sea ice shelves. *Journal of Geophysical Research: Oceans*, *118*(6), 3138–3145. https://doi.org/10.1002/jgrc.20236

Rosevear, M. G., Galton-Fenzi, B., & Stevens, C. (2022). Evaluation of basal melting parameterisations using in situ ocean and melting observations from the Amery Ice Shelf, East Antarctica. *Ocean Science*, *18*(4), 1109–1130. https://doi.org/10.5194/os-18-1109-2022

Rosevear, M. G., Gayen, B., & Galton-Fenzi, B. K. (2022). Regimes and transitions in the basal melting of Antarctic Ice Shelves. *Journal of Physical Oceanography*, *52*(10), 2589–2608. https://doi.org/10.1175/jpo-d-21-0317.1

Rosevear, M. G., Gayen, B., Vreugdenhil, C. A., & Galton-Fenzi, B. K. (2024). How does the ocean melt Antarctic Ice Shelves? *Annual Review of Marine Science*, *29*, 325–353. https://doi.org/10.1146/annurev-marine-040323

Simpson, J. H., & Tinker, J. P. (2007). A test of the influence of tidal stream polarity on the structure of turbulent dissipation. *Continental Shelf Research*, *29*(1), 320–332. https://doi.org/10.1016/j.csr.2007.05.013

Soulsby, R. L. (1983). The bottom boundary layer of shelf seas. In *Physical oceanography of coastal and shelf seas* (pp. 189–266).

Souza, A. J., & Simpson, J. H. (1995). The modification of tidal ellipses by stratification in the Rhine ROFI. *Continental Shelf Research*, *16*(8), 997–1007. https://doi.org/10.1016/0278-4343(95)00042-9

Vaňková, I., Nicholls, K. W., Corr, H. F., Makinson, K., & Brennan, P. V. (2020). Observations of tidal melt and vertical strain at the Filchner-Ronne Ice Shelf, Antarctica. *Journal of Geophysical Research: Earth Surface*, *125*(1), e2019JF005280. https://doi.org/10.1029/2019JF005280

Vaňková, I., & Nicholls, K. W. (2022). Ocean variability beneath the Filchner-Ronne Ice Shelf Inferred from basal melt rate time series. *Journal of Geophysical Research: Oceans*, *127*(10), 20. https://doi.org/10.1029/2022JC018879

Verspecht, F., Simpson, J. H., & Rippeth, T. P. (2010). Semi-diurnal tidal ellipse variability in a region of freshwater influence. *Geophysical Research Letters*, *37*(18), L18602. https://doi.org/10.1029/2010GL044470

Visser, A. W., Souza, A. J., Hessner, K., & Simpson, J. H. (1994). The effect of stratification on tidal current profiles in a region of freshwater influence. *Oceanologica Acta*, *17*(4), 369–381.

Vreugdenhil, C. A., & Taylor, J. R. (2019). Stratification effects in the turbulent boundary layer beneath a melting ice Shelf: Insights from resolved large-eddy simulations. *Journal of Physical Oceanography*, *49*(7), 1905–1925. https://doi.org/10.1175/JPO-D-18-0252.1

Vreugdenhil, C. A., Taylor, J. R., Davis, P. E. D., Nicholls, K. W., Holland, P. R., & Jenkins, A. (2022). The ocean boundary layer beneath Larsen C Ice Shelf: Insights from Large-Eddy Simulations with a Near-Wall Model. *Journal of Physical Oceanography*, *52*(8), 1903–1926. https://doi.org/10.1175/jpo-d-21-0166.1